

**ISTANBUL TECHNICAL UNIVERSITY ★ GRADUATE SCHOOL OF SCIENCE**  
**ENGINEERING AND TECHNOLOGY**

**DEVELOPMENT OF MICROFLUIDIC SYSTEMS FOR DIFFERENTIAL  
SORTING OF MICROPARTICLES AND INVESTIGATION OF THEIR  
PERFORMANCES**



**PhD THESIS**

**Kaan ERDEM**

**Department of Mechanical Engineering**

**Mechanical Engineering Graduate Programme**

**JULY 2020**



**ISTANBUL TECHNICAL UNIVERSITY ★ GRADUATE SCHOOL OF SCIENCE**  
**ENGINEERING AND TECHNOLOGY**

**DEVELOPMENT OF MICROFLUIDIC SYSTEMS FOR DIFFERENTIAL  
SORTING OF MICROPARTICLES AND INVESTIGATION OF THEIR  
PERFORMANCES**



**PhD THESIS**

**Kaan ERDEM**  
**(503132020)**

**Department of Mechanical Engineering**

**Mechanical Engineering Graduate Programme**

**Thesis Advisor: Prof. Dr. Lütfullah KUDDUSİ**  
**Thesis Co-Advisor: Prof. Dr. Ali KOŞAR**

**JULY 2020**



**ISTANBUL TEKNİK ÜNİVERSİTESİ ★ FEN BİLİMLERİ ENSTİTÜSÜ**

**MİKRO PARTİKÜLLERİN AYRIŞTIRILMASI İÇİN MİKRO AKIŞ  
SİSTEMLERİNİN GELİŞTİRİLMESİ VE PERFORMANSLARININ  
İNCELENMESİ**

**DOKTORA TEZİ**

**Kaan ERDEM  
(503132020)**

**Makina Mühendisliği Anabilim Dalı**

**Makina Mühendisliği Lisansüstü Programı**

**Tez Danışmanı: Prof. Dr. Lütfullah KUDDUSİ  
Eş Danışman: Prof. Dr. Ali KOŞAR**

**TEMMUZ 2020**



Kaan ERDEM, a Ph.D. student of ITU Graduate School of Science Engineering and Technology student ID 503132020, successfully defended the thesis/dissertation entitled “DEVELOPMENT OF MICROFLUIDIC SYSTEMS FOR DIFFERENTIAL SORTING OF MICROPARTICLES AND INVESTIGATION OF THEIR PERFORMANCES”, which he prepared after fulfilling the requirements specified in the associated legislations, before the jury whose signatures are below.

**Thesis Advisor :**      **Prof. Dr. Lütfullah KUDDUSİ** .....  
Istanbul Technical University

**Co-advisor :**          **Prof. Dr. Ali KOŞAR** .....  
Sabancı University

**Jury Members :**      **Prof. Dr. Seyhan UYGUR ONBAŞIOĞLU** .....  
Istanbul Technical University

**Prof. Dr. Fırat Oğuz EDİS** .....  
Istanbul Technical University

**Dr. Öğr. Üyesi Ali DİNLER** .....  
Istanbul Medeniyet University

**Dr. Öğr. Üyesi Murat ÇAKAN** .....  
Istanbul Technical University

**Dr. Öğr. Üyesi Ersin SAYAR** .....  
Istanbul Technical University

**Date of Submission : 9 June 2020**

**Date of Defense : 8 July 2020**





*To my family and friends,*



## **FOREWORD**

The experimental works of this study carried out by utilizing the devices of Sabanci University Nanotechnology Research Center (SUNUM) and Faculty of Engineering and Natural Sciences (FENS) of Sabanci University. Also, this work was supported by the Research Fund of the Istanbul Technical University, Project Number: MDK-2017-40845. I am thankful to Istanbul Technical University and Sabanci University for their valuable contribution to realize this work.

I would like to express my gratitude to my thesis advisors Prof. Dr. Lütfullah KUDDUSİ and Prof. Dr. Ali KOŞAR for their valuable advice and support throughout the study.

Finally, I would like to thank my family and my close friends for their patience, encouragement and support.

JUNE 2020

Kaan ERDEM  
(M.Sc. Mech. Eng.)



## TABLE OF CONTENTS

	<u>Page</u>
<b>FOREWORD</b> .....	<b>ix</b>
<b>TABLE OF CONTENTS</b> .....	<b>xi</b>
<b>ABBREVIATIONS</b> .....	<b>xiii</b>
<b>SYMBOLS</b> .....	<b>xv</b>
<b>LIST OF TABLES</b> .....	<b>xvii</b>
<b>LIST OF FIGURES</b> .....	<b>xix</b>
<b>SUMMARY</b> .....	<b>xxiii</b>
<b>ÖZET</b> .....	<b>xxv</b>
<b>1. INTRODUCTION</b> .....	<b>1</b>
1.1 Literature Reviw of Microfluidic Systems.....	2
1.1.1 Biochemical sorting methods.....	3
1.1.2 Physical sorting methods .....	6
1.2 Unique Aspect.....	10
1.3 Research Structure and Thesis Outline .....	12
<b>2. THEORY</b> .....	<b>13</b>
2.1 Dynamics Forces Acting on a Migrating Particle in Inertial Microfluidics.....	14
2.1.1 Net inertial lift force.....	14
2.1.1.1 Wall-induced lift force .....	15
2.1.1.2 Shear gradient lift force.....	16
2.1.2 Viscous drag force .....	16
2.1.3 Deformability-induced lift force .....	17
2.2 Design Principle .....	17
2.3 Design of the Microchannels .....	20
2.3.1 Cross-sectional shape.....	22
2.3.2 Curvature radius .....	23
2.3.3 Channel length .....	24
2.3.4 Microfiltration design .....	27
<b>3. EXPERIMENTAL METHODS AND DATA ANALYSIS</b> .....	<b>29</b>
3.1 Device Fabrication .....	29
3.1.1 Substrate (SU-8 mold) preparation .....	29
3.1.1.1 Cleaning of the wafers .....	29
3.1.1.2 Spin coating of SU-8.....	29
3.1.1.3 UV light exposure .....	30
3.1.1.4 SU-8 development.....	31
3.1.2 Microchannel fabrication .....	32
3.1.2.1 PDMS casting .....	32
3.1.2.2 O <sub>2</sub> Plasma Treatment.....	34
3.1.2.3 Fabrication issues of microfiltration unit of Case 5 .....	36
3.2 Suspension Preparation .....	40
3.3 Experimental Setup .....	40
3.4 Data Analysis .....	42
3.5 Numerical Simulations.....	42

<b>4. RESULTS AND DISCUSSION.....</b>	<b>45</b>
4.1 Laminar Flow Simulation.....	45
4.1.1 Secondary flow analysis along the microchannels.....	45
4.1.2 The effect of alterations in the radius of curvature .....	46
4.2 Lateral Positioning of Particle Streams .....	47
4.2.1 Determination of optimum flow rates .....	47
4.2.2 Lateral focusing behavior of 10- $\mu\text{m}$ and 20- $\mu\text{m}$ particles.....	49
4.2.2.1 Low range of flow rates ( $Re_C < 70$ ).....	49
4.2.2.2 Mid-range of flow rates ( $70 < Re_C < 160$ ).....	50
4.2.2.3 High range of flow rates ( $160 < Re_C$ ).....	50
4.2.3 Comparison of the focusing behavior of elliptic microchannels.....	51
4.2.4 The change of focusing behavior at the exit of straight outlet .....	52
4.3 Particle Separation Capability .....	52
4.4 Discussion of the Experimental Results Regarding the Numerical Study .....	55
<b>5. CONCLUSIONS.....</b>	<b>59</b>
<b>REFERENCES .....</b>	<b>63</b>
<b>CURRICULUM VITAE .....</b>	<b>71</b>

## **ABBREVIATIONS**

<b>CK</b>	: Cytokeratin
<b>CTC</b>	: Circulating Tumor Cell
<b>DI</b>	: Deioized
<b>DLD</b>	: Deterministic Lateral Displacement
<b>EpCAM</b>	: Epithelial Cell Adhesion Molecule
<b>IAR</b>	: Initial Aspect Ratio
<b>IPA</b>	: Isopropyl Alcohol
<b>N<sub>2</sub></b>	: Nitrogen
<b>O<sub>2</sub></b>	: Oxygen
<b>PDMS</b>	: Polydimethylsiloxane
<b>RBC</b>	: Red Blood Cell
<b>RF</b>	: Radio Frequency
<b>Si</b>	: Silicon
<b>UV</b>	: Ultraviolet
<b>v/v</b>	: Volume to volume ratio
<b>WBC</b>	: White Blood Cell



## SYMBOLS

<b><math>a_p</math></b>	: Particle diameter ( $\mu\text{m}$ )
<b><math>C_L</math></b>	: Lift coefficient (-)
<b><math>De</math></b>	: Dean Number (-)
<b><math>D_h</math></b>	: Hydraulic diameter ( $\mu\text{m}$ )
<b><math>F_D</math></b>	: Drag Force (N)
<b><math>F_L</math></b>	: Lift Force (N)
<b><math>F_s</math></b>	: Shear Gradient Lift Force (N)
<b><math>F_w</math></b>	: Wall Induced Lift Force (N)
<b><math>H</math></b>	: Channel height ( $\mu\text{m}$ )
<b><math>L_D</math></b>	: Dean Migration length (mm)
<b><math>L_I</math></b>	: Channel length required for focusing (cm)
<b><math>L_M</math></b>	: Migration length (mm)
<b><math>p</math></b>	: Pressure (Pa)
<b><math>R</math></b>	: Radius of Curvature (mm)
<b><math>Re_c</math></b>	: Channel Reynolds Number (-)
<b><math>r_x, r_y</math></b>	: Radius components on x and y axes (mm)
<b><math>u</math></b>	: Velocity field (m/s)
<b><math>U_{De}</math></b>	: Dean Velocity (m/s)
<b><math>U_L</math></b>	: Lateral migration velocity (m/s)
<b><math>U_m</math></b>	: Mean fluid velocity (m/s)
<b><math>U_{max}</math></b>	: Maximum fluid velocity (m/s)
<b><math>\rho</math></b>	: Density ( $\text{kg/m}^3$ )
<b><math>\mu</math></b>	: Dynamic viscosity (Pa.s)



## LIST OF TABLES

	<u>Page</u>
<b>Table 2.1:</b> Maximum channel heights based on the particle size for successful focusing. ....	<b>22</b>
<b>Table 2.2:</b> The common geometrical parameters and initial geometrical parameters of the first loop for the design of all cases. ....	<b>23</b>
<b>Table 3.1:</b> Speed settings for spin coater. ....	<b>29</b>
<b>Table 3.2:</b> Exposure Input Data for the Mask Aligner. ....	<b>31</b>





## LIST OF FIGURES

	<u>Page</u>
<b>Figure 1.1:</b> Density based layers of blood.....	2
<b>Figure 1.2:</b> Number of publications about microfluidic sorting systems between 1999 and 2011. ....	3
<b>Figure 1.3:</b> Isolation of CTCs from the blood by utilizing physical and/or biological properties.....	4
<b>Figure 1.4:</b> Fluorescence based sorting method using (a) electrostatic deflection or (b) an air bubble creating pulsed laser. ....	5
<b>Figure 1.5:</b> (a) Membrane filters with random and microfabricated holes capturing cells. (b) Schematic of a pool-dam chip. (c) Schematic of arrays of microposts with gradually narrowing gaps. (d) Captured cancer cells by crescent-shaped traps.....	7
<b>Figure 1.6:</b> Layout of the pinched-flow device used for isolation of CTCs.. ....	8
<b>Figure 1.7:</b> Deterministic lateral displacement: an array of microposts with a row shift fraction of 1:3 utilized for separation of small particles (green path) and large particles (red path).....	8
<b>Figure 1.8:</b> (a) Schematic of a spiral microchannel based on Dean-coupled inertial migration of different size particles along the channel. (b) Microchannel cross-section illustrating the effect of the ratio of net lift force to Dean drag force ( $F_L/F_D$ ) for particles of different sizes, which determines where particles equilibrate based on their diameters. ....	9
<b>Figure 2.1:</b> (a) Equilibrium positions in straight channels. b) Single equilibrium position (near the wall closer to the curvature center) in curved channels and the black vectors represents Dean vortices (secondary flow) [59]...	14
<b>Figure 2.2:</b> Shear gradient (black) and wall-induced (red) lift forces acting on particles. ....	15
<b>Figure 2.3:</b> Wall-induced lift force. ....	16
<b>Figure 2.4:</b> Shear gradient lift force. ....	16
<b>Figure 2.5:</b> a) Dean Flow in a rectangular channel, b) equilibrium position due to Dean flow effects, c) Drag force acting on a suspended particle.....	17
<b>Figure 2.6:</b> (a) Schematic of an elliptic spiral microchannel shown in a Cartesian plane including radius of curvature, $R$ at a random position and the location of A-A' cross-section. (b) A close-up view of A-A' plane illustrating secondary flow induced Dean vortices, zero Dean velocity lines and a force diagram demonstrating the directions of wall induced lift force ( $F_w$ ), shear gradient lift force ( $F_s$ ) and Dean drag force ( $F_D$ ) acting on a particle at various locations. ....	19
<b>Figure 2.7:</b> Schematics of the Elliptic Spiral Microchannels: (a) Case 1 (Initial Aspect Ratio ( $IAR$ ): 3:2), (b) Case 2 ( $IAR$ : 11:9), (c) Case 3 ( $IAR$ : 9:11) and (d) Case 4 ( $IAR$ : 2:3).....	25
<b>Figure 2.8:</b> Dean number variations at the end of the curved section of the elliptic spiral microchannels.....	256

<b>Figure 2.9:</b> Microfiltration platform implemented in Case 5 where the diameter of the microposts is 60 $\mu\text{m}$ and the gap is 40 $\mu\text{m}$ with row shift fraction of 1:10.....	<b>28</b>
<b>Figure 3.1:</b> Spin Coater with the control panel. ....	<b>30</b>
<b>Figure 3.2:</b> Acetate Photomask. ....	<b>30</b>
<b>Figure 3.3:</b> Mask Aligner 4". ....	<b>31</b>
<b>Figure 3.4:</b> An example of a microchannel surface profile (Case 1). ....	<b>32</b>
<b>Figure 3.5:</b> SU-8 Mold ready for PDMS Casting. ....	<b>33</b>
<b>Figure 3.6:</b> Degassing in the vacuum oven. ....	<b>33</b>
<b>Figure 3.7:</b> PDMS cast after baking and removing from the SU-8 mold. ....	<b>34</b>
<b>Figure 3.8:</b> Punching the inlet and outlet holes on PDMS. ....	<b>34</b>
<b>Figure 3.9:</b> Harrick Plasma Cleaner. ....	<b>35</b>
<b>Figure 3.10:</b> Gas Flow Mixer( PlasmaFlo). ....	<b>35</b>
<b>Figure 3.11:</b> Purple glow during oxygen plasma treatment. ....	<b>36</b>
<b>Figure 3.12:</b> Microscopic images of the photomask of the microfiltration unit of 30 $\mu\text{m}$ posts under (a) 5x, (b) 10x, (c) 20x zoom. ....	<b>37</b>
<b>Figure 3.13:</b> Microscopic images of the SU-8 mold of the microfiltration unit consisting of 30 $\mu\text{m}$ posts under 10x and 20x zoom. ....	<b>37</b>
<b>Figure 3.14:</b> Microscopic image of the microfiltration unit made of PDMS consisting of 30 $\mu\text{m}$ -wide and 90 $\mu\text{m}$ -high posts under 20x zoom with dimensioning. ....	<b>38</b>
<b>Figure 3.15:</b> Underdevelopment issue in Case 5 with 60- $\mu\text{m}$ wide microposts.....	<b>39</b>
<b>Figure 3.16:</b> (a) The rupture of microposts and (b) the clogging in Case 5 with 90- $\mu\text{m}$ wide microposts. ....	<b>39</b>
<b>Figure 3.17:</b> Experimental Setup.....	<b>40</b>
<b>Figure 3.18:</b> Connection of single inlet and 8 outlet openings with corresponding tubings and fittings. ....	<b>41</b>
<b>Figure 3.19:</b> Uniform hexahedral mesh used in numerical simulations.....	<b>42</b>
<b>Figure 4.1:</b> (a) Six different cut-plane positions labeled starting from the inner loop along the primary flow direction, and (b) a closer look at the vectoral variation of lateral velocity distributions over the colored velocity profile of the primary flow at six different cross sections throughout the channel. The cross-sectional velocity profiles were retrieved from COMSOL Multiphysics simulation results of Case 1 (IAR=3:2) at the volumetric flow rate of 3 mL/min. ....	<b>45</b>
<b>Figure 4.2:</b> The variations of Dean velocity distribution at the beginning and at end of the last quarter loop of the channel for a and b) Case 1 (IAR=3:2), c and d) Case 2 (IAR=11:9), e and f) Case 3 (IAR=9:11) and g and h) Case 4 (IAR=2:3), respectively. The arrow lengths are proportional to the lateral velocity. ....	<b>46</b>
<b>Figure 4.3:</b> Lateral focusing position from the inside wall normalized by the channel exit width of 1mm for a) Case 1 (IAR=3:2), b) Case 2 (IAR=11:9), c) Case 3 (IAR=9:11) and d) Case 4 (IAR=2:3) at the outlet.....	<b>48</b>
<b>Figure 4.4:</b> The trajectories of the particle streamlines at the end of the last spiral loop, where the channel width is 500 $\mu\text{m}$ for 10 $\mu\text{m}$ (red lines) and 20 $\mu\text{m}$ (green lines) at $Re_C$ of 63, 126 and 188 for a) Case 1 (IAR=3:2), b) Case 2 (IAR=11:9), c) Case 3 (IAR=9:11) and d) Case 4 (IAR=2:3).. ....	<b>48</b>
<b>Figure 4.5:</b> The superimposed fluorescent image of the focused streamlines: red (10 $\mu\text{m}$ ) and green (20 $\mu\text{m}$ ) illustrating particle migration for Case 4 (IAR=2:3) at the optimum flow conditions ( $Re_C=195$ ). ....	<b>51</b>

**Figure 4.6:** (a) The fluorescent microscopic views of samples utilized for particle counting and (b) the superimposed fluorescent image of two focused streamlines: red ( $10\mu\text{m}$ ) and green ( $20\mu\text{m}$ ) illustrating particle migration for Case 4 (IAR=2:3) at the optimum flow conditions ( $Re_c=195$ ). ..... **533**

**Figure 4.7:** The particle separation purities obtained from the ratio of collected particles at particular outlets to the total collected particles for outlet #1 and #2 in a) Case 1 (IAR=3:2), b) Case 2 (IAR=11:9), c) Case 3 (IAR=9:11) and d) Case 4 (IAR=2:3). ..... **54**





# **DEVELOPMENT OF MICROFLUIDIC SYSTEMS FOR DIFFERENTIAL SORTING OF MICROPARTICLES AND INVESTIGATION OF THEIR PERFORMANCES**

## **SUMMARY**

Inertial microfluidics, an emerging tool in scientific studies, offers rapid, continuous, and high-throughput cell/particle separation. They can be mainly utilized in various applications such as blood separation, the isolation of cancer cells (Circulating Tumor Cells), disease diagnostics and monitoring, and biological processes. For the isolation of targeted particles or cells at the micro scale, a variety of methods has been proposed. Among these methods, label-free, size-dependent cell-sorting applications based on inertial focusing phenomena have attracted much interest during the last decade.

In this thesis, five-loop spiral microchannels with a height of 90  $\mu\text{m}$  and a width of 500  $\mu\text{m}$  are introduced. Unlike their original spiral counterparts, four of the proposed channels have elliptic configurations of differing elliptic aspect ratios of 3:2, 11:9, 9:11, and 2:3. Accordingly, the curvature of these configurations increases in a curvilinear manner through the channel. Additionally, the other of proposed microchannel differs due to the implementation of a filtration platform consisting of cylindrical microposts. Both microchannels were designed in order to improve the separation capability.

The proposed microchannels were fabricated by using the standard soft lithography method. As channel material, PDMS (polydimethylsiloxane) was utilized. The steps of the microfabrication process were adjusted in order to meet the predetermined geometical features. The fabrication of the cylindrical microposts was challenging due to several reasons such as low quality of printed photomasks, loss of some microposts during PDMS cast (channel material) removal and clogging problem by dust and debris in the experiments. Therefore, the study was carried out with the elliptic configurations.

The effects of the alternating curvature and the channel Reynolds number on focusing of fluorescently dyed particles with diameter of 10 and 20  $\mu\text{m}$  in the prepared suspensions were investigated by using the fabricated microchannels. After focusing particles at distinctive positions across the microchannel, the optimum volumetric flow rates between 0.5 mL/min and 3.5 mL/min allowing separation were determined for each channel. These flow rates were specified by utilizing the captured microscopic image sequences of the particle migration trajectories at the outlet. At these rates, each channel was tested in order to collect samples at the designated outlets. Then, these samples were analyzed by counting particles visually under a fluorescence microscope to determine the separation purity. As a result, these elliptic microchannels were capable of separating 20 and 10  $\mu\text{m}$  particles with total yields up to approximately 95% and 90%, respectively. The results exhibited that the level of enrichment and the focusing behavior of the proposed configurations are promising compared to the existing microfluidic channel configurations. A research article related to this study

has been published in a peer-reviewed journal that is indexed by the Science Citation Index Expanded (Web of Science) and Scopus (citescore quartile Q2).

Considering their advantages as high operating flow rates, non-complex configuration, and less expensive process requirements, these microfluidic devices offer cost-effective and high-throughput prototypes for efficient separation of microparticles/cells such as CTCs, blood cells, bacteria, viruses, etc. and could be further customized for various sorting applications.



# MİKRO PARTİKÜLLERİN AYRIŞTIRILMASI İÇİN MİKRO AKIŞ SİSTEMLERİNİN GELİŞTİRİLMESİ VE PERFORMANSLARININ İNCELENMESİ

## ÖZET

Son yıllarda bilimsel çalışmalar kapsamında geliştirilen, atalet kuvvetlerine dayalı mikro akış sistemleri hızlı, sürekli ve yüksek verimli hücre/partikül ayırıştırma imkanı sunmaktadır. Bu sistemlerden kan hücrelerinin ayırıştırılması, kanda dolaşan kanserli hücrelerin izole edilmesi, hastalık teşhisinin konulup seyrinin takip edilmesi ve biyolojik prosesler gibi farklı uygulamalarda yararlanılmaktadır. Bu zamana kadar mikro ölçekte hedef partiküllerin ya da hücrelerin izole edilerek ayırıştırılması için çeşitli yöntemler geliştirilmiştir. Bu yöntemler harici bir kuvvet uygulanması durumuna göre aktif ve pasif olarak sınıflandırılmaktadır. Harici kuvvet uygulanan aktif sistemler daha hassas ayırıştırma sağlarlar da yüksek proses maliyetleri, düşük çalışma hızları ve karmaşık konfigürasyonları sebebiyle pasif sistemlerin yanında dezavantajlı konuma düşmektedir. Pasif yöntemler arasında sadece atalet kuvvetlerine dayalı odaklamayı temel alan, boyut bazlı, partiküllere ya da hücrelere biyokimyasal imleme (etiketleme) yapılmadan ayırıştırma yapılan uygulamalar son yıllarda oldukça önem kazanmıştır.

Bu tez çalışması kapsamında yüksekliği 90  $\mu\text{m}$  ve genişliği 500  $\mu\text{m}$  olan dikdörtgen kesitli, 2 giriş ve 8 çıkışlı, 5 tur spiral döngülü mikrokanallar geliştirilmiştir. Pasif sistemlerde genel olarak süspansiyon içinde yer alan partiküllere sıvının kanal içinde dolaşımı sırasında hidrodinamik kuvvetler etki etmektedir. Bu kuvvetlerin etkisinde partiküllerin boyutlarına göre odaklanması ve ayırıştırılması pasif sistemlerin temelini oluşturmaktadır. Doğrusal kanallarda partiküllere ataletlerinden kaynaklanan kaldırma ve sürüklenme kuvvetleri etki etmektedir. Bu kanallarda sürüklenme kuvveti akış doğrultusunda etkili olduğu için partiküllerin odaklanmasında akışa dik doğrultuda etkiyen kaldırma kuvvetleri rol oynamaktadır. Cisme uygulanan kaldırma kuvveti temel olarak birbirine ters yönde etkiyen kayma gerilmesi (hız gradyanı) ve duvar etkisi kaynaklıdır. Kayma gerilmesi kaynaklı kaldırma kuvveti, akışkanın parabolik hız profili sebebiyle partikül etrafında meydana gelen bağıl hız farkının dengelenmesi için kanal merkezinden duvarlara doğru etki etmektedir. Duvar etkisi kaynaklı kaldırma kuvveti ise partikül ve duvar arasında sıkışan akışkanın yarattığı basınç ile duvardan merkeze doğru etki yaratmaktadır.

Dikdörtgen kesitli kanallarda bu iki kaldırma kuvvetinin etkisinde partiküller kanal içinde 4 farklı pozisyonda hizaya gelmektedir. Spiral kanallarda ise eğriliğin yarattığı atalet akışa dik düzlemde ikincil bir akış meydana getirmektedir. Bu ikincil akış etkisinde Dean sürüklenme kuvveti olarak adlandırılan ikincil bir sürüklenme kuvveti oluşmaktadır. Dikdörtgen kesitli eğrisel kanallarda hem Dean sürüklenme kuvveti hem de net kaldırma kuvveti etkisi altındaki partiküller kanal içinde tek bir pozisyonda odaklanmaktadır. Bu pozisyon partikülün boyutuna göre değişiklik göstermesi

prensibinden yararlanarak farklı boyutlu partiküllerin ayrıştırılması gerçekleştirilmektedir.

Orijinal spiral kanallardan farklı olarak bu çalışma kapsamında toplam 7 farklı kanal geliştirilmiştir. Bu geliştirilen kanallardan dördü eliptik konfigürasyona sahiptir. Bu konfigürasyonlardaki elips formuna ait en-boy oranı 3:2, 11:9, 9:11 ve 2:3 olacak şekilde her bir kanal için değişmektedir. Eliptik konfigürasyonun sonucu olarak eğrilik yarıçapı kanal boyunca dalgalı bir şekilde artış göstermektedir. Benzer şekilde eğrilik yarıçapı ile birlikte ikincil sürüklenme kuvveti de dalgalı olarak değişim göstermekte ve bu durumun partiküllerin yanal hareketlerini etkileyerek hizaya gelmelerini hızlandırması öngörülmektedir.

Bu 4 kanala ek olarak, geliştirilen diğer 3 spiral kanalda ise silindirik mikro sütunların yer aldığı bir filtreleme platformu dahil edilmiştir. Mikro sütun çapları 30, 60 ve 90 µm olarak tasarlanmıştır. Mikro sütunlar 1:10 açıyla dizilerek tıkanma meydana gelmeden partiküllerin boyut bazlı filtrelenmesi ve böylelikle spiral kanallarda gerçekleşen atalet kuvvetlerine dayalı ayrıştırmanın desteklenmesi hedeflenmiştir. Genel olarak mikrokanalların hepsi ayrıştırma kapasitesini iyileştirme amacıyla tasarlanmış ve performansları incelenmiştir. Tez kapsamında 4 eliptik kanal 4 ayrı durum olarak ele alınırken filtreleme platformu içeren 3 kanal tek bir durum olarak ele alınmıştır.

Standard litografi yöntemi kullanılarak mikrokanalların üretimi yapılmıştır. Tasarlanan kanalların geometrileri yüksek çözünürlüklü yazıcıda asetat üzerine bastırılarak foto maskeler üretilmiştir. Foto maske yardımı ile kanal konfigürasyonu silikon plaka üzerine kaplanan SU-8 kalıba aktarılmıştır. Litografi yöntemine ait işlem basamakları istenilen geometrileri elde edecek şekilde düzenlenmiştir. Kanal üretiminde malzeme olarak PDMS (polidimetilsiloksan) kullanılmıştır. Kalıptan çıkarılan PDMS uygun boyuttaki mikroskop lam ile bağlanarak kapalı mikrokanal formu oluşturulmuştur. Silindirik mikro sütunların üretimi ise birtakım sebeplerden ötürü zorluk yaratmıştır. Bu sebepler foto maskelerin baskı kalitesinin yetersiz kalması, dökümü yapılan PDMS kalıptan çıkarılırken bazı sütunların kopması ve toz ve parçacıklar sebebiyle deney esnasında tıkanma gerçekleşmesi olarak sıralanabilir. Yukarıda açıklanan sebeplerden dolayı çalışmanın kalanına eliptik mikrokanallarla devam edilmiştir.

Üretilen mikrokanallarda değişen kanal eğrilik yarıçapının ve Reynolds sayısının 10 ve 20 µm çaplı, floresan boyalı partiküllerin fokuslanması üzerine etkileri incelenmiştir. Deiyonize su ile karışımı hazırlanan partiküller kanal içinde ayırt edici pozisyonlarda fokuslanarak 0.5 mL/dk ve 3.5 mL/dk aralığında verimli ayrıştırmanın gerçekleşebileceği en uygun hacimsel debi belirlenmiştir. Bu işlem her bir eliptik kanal için tekrarlanmıştır. Bu debileri belirlerken kanalların çıkışında partiküllerin izlediği yollara ait alınan mikroskopik görüntü kayıtlarından yararlanılmıştır. Bu kayıtlardan yararlanarak 0.5mL/dk aralıklarla her debide 10 ve 20 µm çaplı partiküller için fokuslanma aralıkları belirlenmiş ve üst üste çakışmanın olmadığı ve ayrıştırma yapımına en uygun debiler tayin edilmiştir. Yaklaşık olarak 3mL/dk civarında 4 eliptik kanalda da ayrışmanın gerçekleşebildiği gözlenmiştir.

Belirlenen bu debilerde her bir kanal için partikül sayım testi gerçekleştirilmiştir. Tayin edilen çıkış kanallarından süspansiyon içindeki partiküller toplanmıştır. Daha sonra toplanan örneklerden küçük numuneler lamel üzerine aktarılarak partikül sayımı floresan mikroskop altında gözle yapılmıştır. Daha doğru sonuç almak adına bu işlem defalarca tekrarlanmıştır. Sayımlar 8 çıkış için de gerçekleştirilmiştir. Tüm çıkışlardan

elde edilen partikül miktarı toplam miktara oranlanarak 10 ve 20 µm çaplı partiküller için ayrıştırma verimleri hesaplanmıştır. Sonuç olarak bu çalışmada sunulan eliptik mikrokanallar 20 ve 10 µm çaplı partiküller için sırasıyla %95 ve %90'a varan ayrıştırma verimi göstermiştir. Halihazırda var olan mikrokanallarla kıyaslandığında bu kanalların partikül odaklama ve ayrıştırma açısından daha iyi sonuçlar verdiği görülmüştür. Böylece herhangi bir dış güce ihtiyaç olmaksızın sadece eliptik formun partiküllerin yanıl hareketine olumlu etkisiyle ayrıştırma veriminin iyileştiği gösterilmiştir. Floresan boyalı mikropartiküllerle elde edilen bu sonuçlara dayanarak, geliştirilen eliptik mikrokanallardan kanda dolaşan kanserli hücrelerin ayrıştırıldığı uygulamalarda da faydalanılması uygundur.

20 µm çaplı partiküller için %95.3 verimle en iyi ayrıştırma en-boy oranı 9:11 olan kanalda meydana gelmiştir. Diğer yandan 3:2 en-boy oranına sahip kanalda 90.0% verimle 10 µm çaplı partiküller daha iyi ayrıştırma gerçekleşmiştir. Sadece 10 µm çaplı partikülleri ayırmak ya da 10 ve 20 µm çaplı partikülleri birbirinden ayırtmak için en iyi alternatifin her partikül için %90 üzerinde verim sağlayan ve en-boy oranı 3:2 olan eliptik kanal olduğu sonucuna varılmıştır. Sadece 20 µm çaplı partiküllerin izole edilmek istendiği uygulamalarda ise 9:11 en-boy oranına sahip eliptik kanalı değerlendirmek daha doğru olacaktır.

Deneysel çalışmada geniş hacimsel debi aralığında test yapma imkanı sağlaması için kanallar ihtiyaç duyulandan daha uzun tasarlanmıştır. Bu uygulama kapsamında optimum debilerin yüksek değerlerde olduğu tespit edilmiştir. Yüksek debilerde partiküllerin odaklanması için gerekli olan kanal uzunluğu daha kısadır. Eliptik kanalların spiral döngü sayıları azaltılarak kapladıkları alanlar küçültülebilir. Böylelikle üretim maliyeti de büyük ölçüde düşürülebilir. Yüksek debilerde çalışmanın bir diğer faydası ise kısa sürede daha fazla miktarda partikül ayrıştırma imkanı sağlamasıdır.

Ayrıştırmanın gerçekleştiği en uygun debilerde, 10 ve 20 µm çaplı partiküllerin odaklandığı pozisyonlar arasındaki boşluğun kısmen geniş olduğu tespit edilmiştir. Kanal genişliği daraltılarak hem bu boşluk kapatılabilir hem de kanalın kapladığı alan küçültülebilir. Fakat bu durumda kanal yüksekliğinin kanal genişliğine oranı artacağı için Dean sürüklenme etkileri artacağından ayrıştırma kapasitesi açısından istenmeyen sonuçlar meydana gelebilir. Yine de fokus bantları arasındaki bu boşluk ileriki çalışmalarda boyutları birbirine daha yakın partiküllerin ayrıştırılması için fırsat doğurmaktadır.

Deneysel taşıyıcı akışkan olarak deiyonize su kullanılmıştır. Gelecekte ayrıştırma etkinliğini arttırmak için Newton tipi akışkan su yerine Newton tipi olmayan akışkanlar deneyerek elastik kaldırma kuvveti sisteme dahil edilebilir ve ayrıştırma performansında etkisi incelenebilir.

Kanallar sadece tek sefer işleme tabi tutularak yüksek verimler sağlamıştır. Ardışık/paralel uygulamalar ile verim değerleri daha da yükseltilebilir. Bu çalışma kanal çıkışındaki odaklanma mekanizması ve ayrıştırma performansına ışık tutsa da kanal boyunca partiküllerin hareketleri incelenerek çalışmanın kapsamı genişletilebilir.

Yüksek operasyon hızı, basit konfigürasyon ve düşük proses maliyeti ihtiyacı gibi avantajları göz önünde bulundurulursa, bu çalışmada geliştirilen mikro akış sistemleri çeşitli ayrıştırma uygulamaları için uygun bir ön çalışma oluşturmaktadır. Bu kanallar yardımıyla kanda dolaşan kanserli hücreler, kan hücreleri, bakteriler, virüsler, vb. için düşük bütçe ve yüksek işlem hacmiyle verimli bir ayrıştırma sağlayacak sistemler

kolayca geliştirilebilir. Bu çalışmada elde edilen sonuçlar ile ilgili özgün bir bilimsel makale uluslararası indeksli (Scopus Q2 sınıfı, SCI-EXP) ve hakemli dergide yayımlanmıştır.



## 1. INTRODUCTION

Metastasis is a leading factor for the majority of cancer related deaths [1]. Circulating tumor cells (CTCs) are the precursor of metastatic diseases. The presence of rare CTCs in the peripheral blood has been reported since the 19th century [2]. The metastatic mechanism is run by a CTC going through a series of processes. First, the CTC segregates from the primary malignant tumor and joins the bloodstream. By suspending in the blood circulation, the CTC can easily implant at distant sites, which leads to the formation of a metastatic lesion, known as hematogenous spread [3, 4]. Therefore, the detection, enumeration and characterization of CTCs hold great promise to (i) diagnose at an early stage, (ii) determine individualized treatment by assessing patients' responses to different therapeutic regimens (iii) monitoring cancer progression or relapse and (vi) evaluate cancer stage [5].

CTCs are identified in the circulation system of many patients with cancer types such as colon [6], prostate [7], lung [8], breast [9], nervous system [10], gastric [11], and bladder [12]. It is clinically validated that the amount of CTCs flowing within the blood stream of cancer patients is a good measure for prognostic purposes. Several clinical studies documented the correlation between the detection of CTCs in patients who have the localized primary tumor and subsequent metastatic relapse [13, 14]. It was also reported that the survival of metastatic cancer patients was highly dependent on CTC counts in the bloodstream [15, 16]. Moreover, CTC analysis using blood samples can be occupied in a follow-up of the treatments as a biopsy in a liquid form by letting a molecular characterization of the circulating tumor cells [17].

Whole blood analysis is one of the main interests in diagnosis, treatment and clinical research. Blood is a multi-component suspension, containing 55% of plasma, 44% of red blood cells (RBCs), less than 1% of white blood cells (WBCs). Subjecting the blood sample to centrifugation results in the apparent density gradient layered zones (Figure 1.1). The particles such as RBC and neutrophils will remain under the suspension of CTCs, mononuclear WBCs and plasma due to the density difference [18]. CTCs are rare events in the bloodstream, with a concentration of approximately

1 CTC per  $10^5$ – $10^7$  mononuclear blood cells [19], which have a single nucleus. This makes the detection of CTCs challenging.

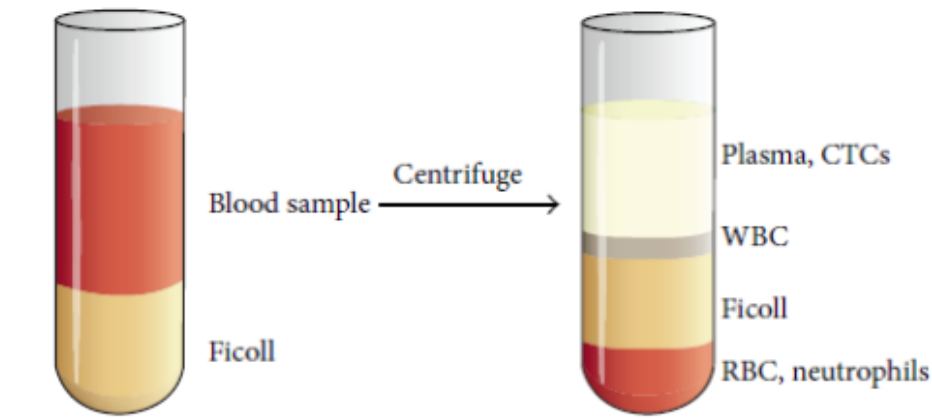


**Figure 1.1:** Density based layers of blood [18].

To capture and analyze the CTC population, numerous microfluidic devices have been developed. These devices vary from those that rely on the isolation of cells based on the expression of cell surface markers to those that rely on excluding the other cells in peripheral blood from CTCs by utilizing distinctive physical properties, thus called label-free selection. The current technologies face technical and biological hurdles limiting their broad utility, therefore available methods for sorting a particular subpopulation such as CTCs remain challenging and offer great research topics.

### 1.1 Literature Review of Microfluidic Systems

The identification of rare cells such as CTCs in a vast amount of surrounding blood cells has been centered upon lately. Thus, microfluidic systems increasingly expand their range and applicability for applications in the rare cells manipulation operations. Thus, microfluidic systems become a tool that has a great contribution to the field from fundamental research to clinical diagnosis. A variety of novel concepts for microfluidics has been proposed and investigated widely during the last two decade and the number of publications have been increasing drastically (Figure 1.2). Hence, this topic offers wide study options since it is a relatively new area of interests for multi disciplinary researchers.

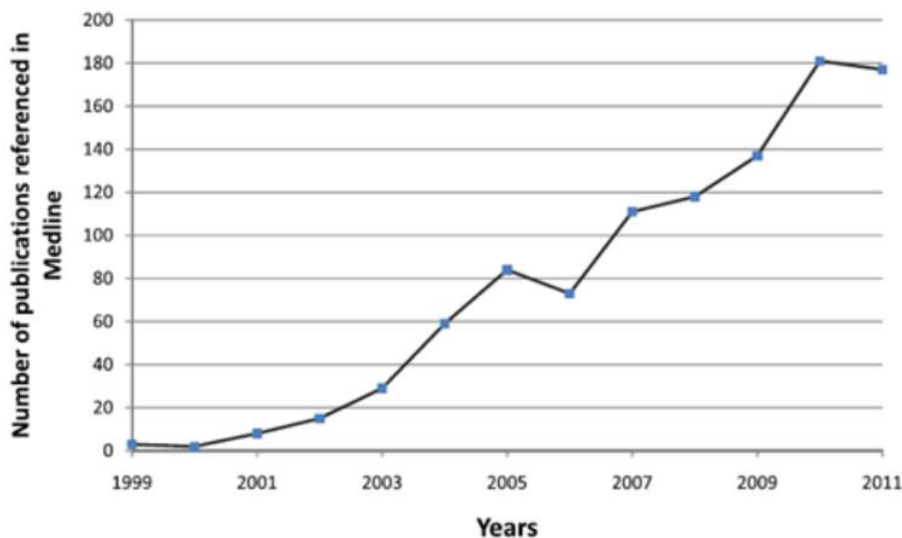


**Figure 1.2:** Number of publications about microfluidic sorting systems between 1999 and 2011 [20].

The current cell sorting methods via microfluidics can be comprehensively categorized into physical and biochemical methods (Figure 1.3) [20, 21]. The physical methods (e.g., size [22], dielectric properties [23], optical properties [5] or deformability [24] based methods), also called label-free, are relatively easy to perform, but are not as specific and sensitive as the biochemical counterparts. On the other hand, biochemically enhanced concepts mainly require the usage of the biomarkers as cytokeratins (CKs) and epithelial cell adhesion molecules (EpCAM) [25], expressed by tumor cells of epithelial origin. In addition to biomarker requirements, the biochemical methods are relatively slower; therefore, they take a longer time for processing.

### 1.1.1 Biochemical sorting methods

Biochemical sorting methods, also known as antibody-based methods mainly built upon the specificity of antibody (marker) and antigen bond. Such methods are popular and relatively effective approaches for the detection and isolation of circulating tumor cells. The performance of a method essentially depends on the employed marker. Therefore, several markers have been investigated. Among all, EpCAM and various subtypes of CK are the most commonly used antigens. The antibody-based methods can be classified as fluorescence, immunomagnetic, and adhesion-based methods.

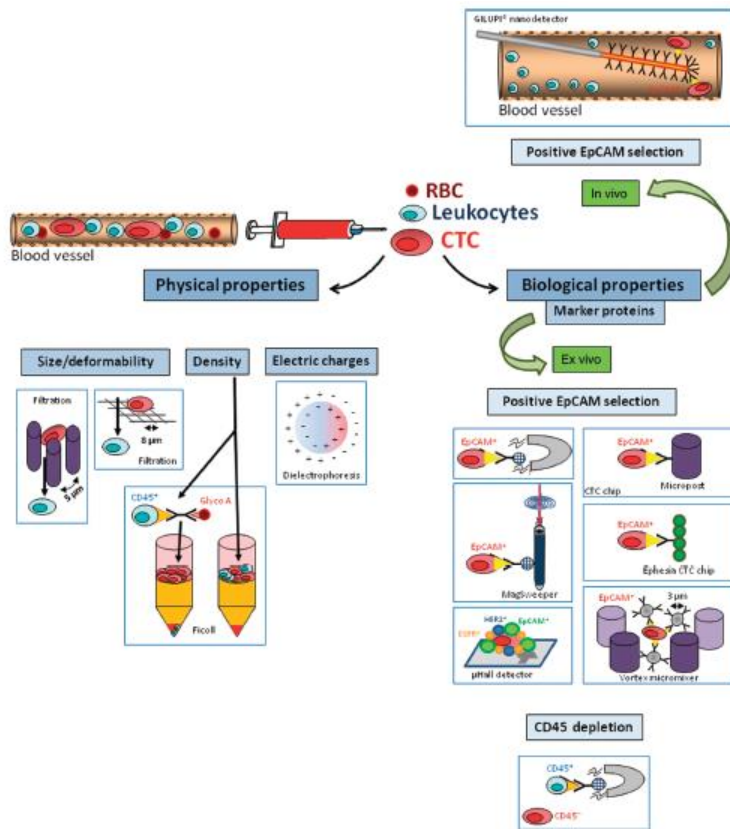


**Figure 1.3:** Isolation of CTCs from the blood by utilizing the physical and/or biological properties. [26].

In fluorescence sorting, each cell is individually lined up and is fed into a nozzle using flow cytometry. Then the cells pass through one or multiple laser beams at high speeds [27]. Following that, cameras sense the fluorescence emitted by the stained cell. Sensors receive both forward and side scatter signals. Afterwards, electrically charged droplets are separated using electrostatic deflection (Figure 1.4(a)) [28]. Additionally, a new technology has been developed with a pulsed laser. When the target cell is detected, the system creates a small air bubble to manipulate these cells into the collection outlet [29] (Figure 1.4(b)).

The underlying principle of immunomagnetic cell separation is the bind between antigens expressed on the cell surface and antibodies attached to magnetic beads. In this approach, target cells are labeled with antibody-grafted magnetic beads (diameter: 0.5–5 µm) or nanoparticles (diameter: 50–250 nm) that usually bind to a certain surface antigen [30]. Then, labeled cells are discriminated from unlabelled cells with the help of magnetic field exposure. Depending on the bead size, the magnetic force deviates in a microfluidic device placed inside an electromagnet creating a permanent magnetic field, leading the labeled cells to migrate towards the designed direction. The

immunomagnetic procedures are performed by using antibodies against either tumor-related antigens (positive selection) or the common white blood cell antigen CD45 (negative selection). EpCAM has often been used for positive selection, as the most common enrichment method employing antibodies against the EpCAM of cell surfaces. Labeling CTCs with anti-EpCAM-coated beads were tested widely [31, 32]. In the negative selection approach, CTCs are negatively isolated by first disintegrating RBCs and then using custom antigens to magnetically withdraw WBCs from the sample [33, 34]. Thus, CTC leaves the process untouched.

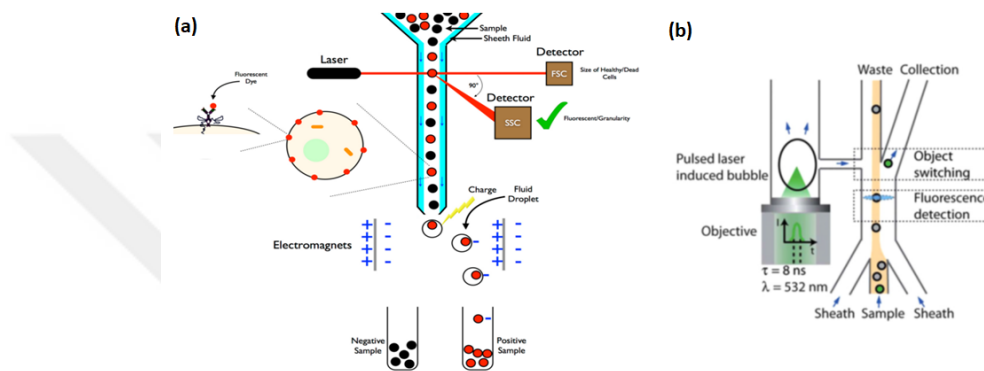


**Figure 1.4:** Fluorescence based sorting method using (a) electrostatic deflection [28] or (b) an air bubble creating pulsed laser [29].

Differently from immunomagnetic counterparts, adhesion-based methods isolate CTCs without any cell labeling. They function either in static (batch-wise) or in flow modes. Yet, isolation from a flowing sample is by far more efficient and common [30]. CTCs can differ from blood cells with respect to the surface marker expressions. Mostly well-characterized antibody-antigen pairs (e.g. anti-EpCAM and EpCAM) are utilized to capture targeted molecules [35-37]. Theoretically, CTCs are captured and retained by flowing across the device coated with surface markers while the rest of the blood cells carry on with the flow. The flow rate should be reasonably slow to ensure maximum cell attachment to the surface. In addition, the broad surface area enhances the possibility of interaction sites and thus CTC capture. Another way of enhancing cell-surface interaction is chaotic micromixers [38].

Overall, there are several important limitations to the usage of the biochemical sorting methods which are high fabrication and operational costs and design complexity. There may also occur contamination and clogging as well. Additionally, the throughput required for continuous separation of CTCs from blood is restricted

regarding the requirement of slow process rates for efficient sorting. Also, these methods require pre-staining of the cell or the surface. This also concludes in increased processing time and consequently potential cell viability loss.

### **1.1.2 Physical sorting methods**

For the isolation of targeted cells or particles at the micro scale, a variety of methods has been proposed. The physical sorting methods can be classified into two categories based on the external power requirement: active and passive separation. Many active separation devices, which depend on external forces such as acoustophoresis [7], dielectrophoresis [39, 40], and optical interference [41] have been developed utilizing the related physical properties (e.g. dielectric properties) and tested. Even though these methods provide more accurate results, they have disadvantages of processing small samples at low operating flow rates, complex integration, and expensive process requirements [42]. However, passive methods simply exploit inherent hydrodynamic forces and physical properties and offer cost-effective and high-throughput alternatives. The passive methods will be described in detail below.

Red blood cells (RBC), also called erythrocyte, have biconcave disk shape with a diameter of approximately 6-8  $\mu\text{m}$  [43]. White blood cells (WBC), also known as leukocytes, are split into two categories, which are granulocytes and agranulocytes. The granulocytes are neutrophils and eosinophils and they have a diameter of 12 to 15  $\mu\text{m}$  [44]. Additionally, the size of the agranulocytes varies between 7–10  $\mu\text{m}$  for small lymphocytes. Meanwhile, large lymphocytes are approximately 14–20  $\mu\text{m}$  in diameter. Monocytes are the largest of the WBCs with a diameter of 15 to 25  $\mu\text{m}$  [43, 44]. Contrary to the blood cell dimensions explained above, the size of CTCs reported and confirmed by several researchers in the literature is generally larger than normal blood cells, varying from 17  $\mu\text{m}$  to 52  $\mu\text{m}$  [45-47]. Even though the difference in the size of CTCs compared to other blood cells has been exploited in several devices as the primary label-free separation criteria, there is an overlap in the size of CTCs and large leukocytes that may affect the efficacy of size-based separation process. Noteworthy, the elasticity of metastatic cells (Young's Modulus: 3.7 kPa –150 kPa) was reported relatively small when compared to blood cells (Young's Modulus: 0.2 kPa) [48].

Due to the fact that tumor cells tend to be larger and stiffer than blood cells [30,48], numerous microfluidic systems (Figure 1.5) have been developed to isolate CTCs by virtue of their size such as track-etched membrane filters, micro barriers (e.g., capillaries), microstructured pool-dam design [49] and array of trappings [6, 24]. These applications have been used to isolate CTCs from the peripheral blood by their size and deformability differences and such designs face the problem of cell accumulation resulting in clogging.

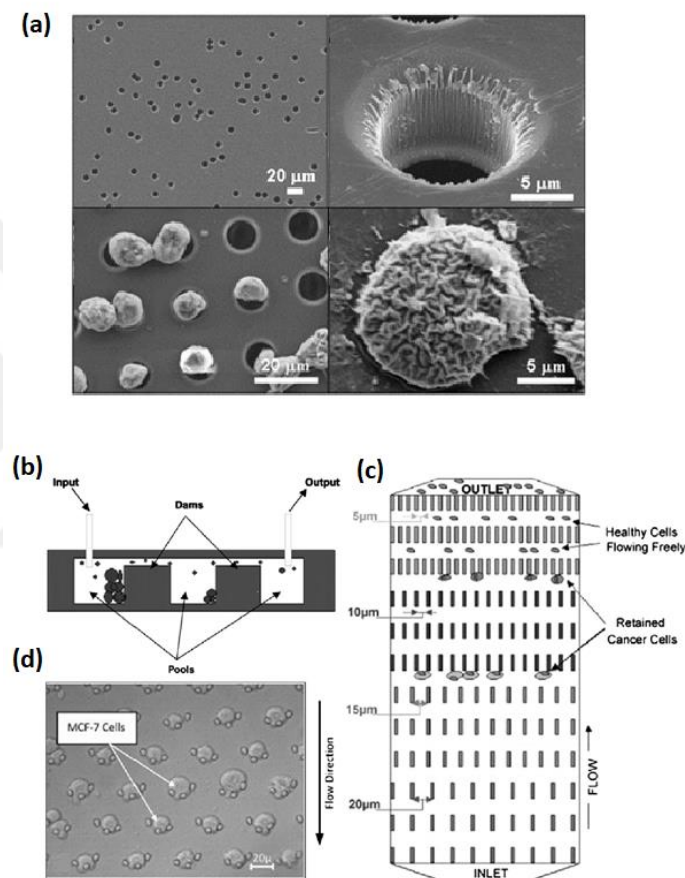


**Figure 1.5:** (a) Membrane filters with random and microfabricated holes capturing cells [30]. (b) Schematic of a pool-dam chip [49]. (c) Schematic of arrays of microposts with gradually narrowing gaps [24]. (d) Captured cancer cells by crescent-shaped traps [6].

Microfluidic flow fractionation is another passive cell sorting approach. The concept combines the effect of hydrodynamic focusing and pinched flow in a microfluidic [50, 51]. The inertial lift force is generated by contribution of contraction–expansion platform through the microchannel, which manipulate cells to form a pinched flow where small cells migrate close to sidewalls and large cancer cells stream in the middle

(Figure 1.6) enabling the target cells to be collected at the desired exit (recovery rate: ~80–90%) [50, 51].

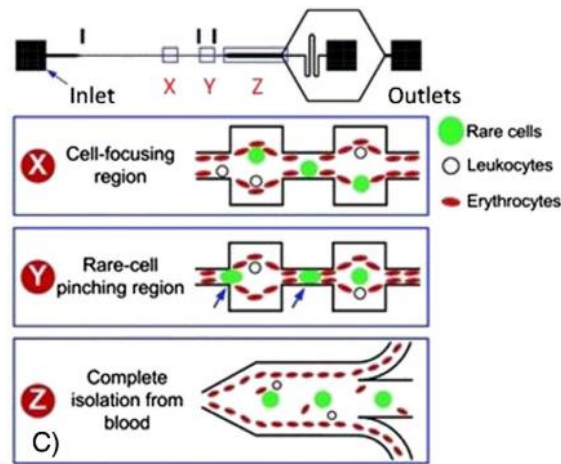


**Figure 1.6:** Layout of the pinched-flow device used for isolation of CTCs. [48].

Another approach is Deterministic Lateral Displacement (DLD) (Figure 1.7). When Reynolds number is low, there are mostly no inertial effects. At low Reynolds numbers, particles suspended in a streamline have a deterministic behavior and follow the streamline, superposed with its intrinsic Brownian motion. By pillar-shaped obstacles, so called microposts, in the way of the particles, the behavior changes depending on the size of the particle.

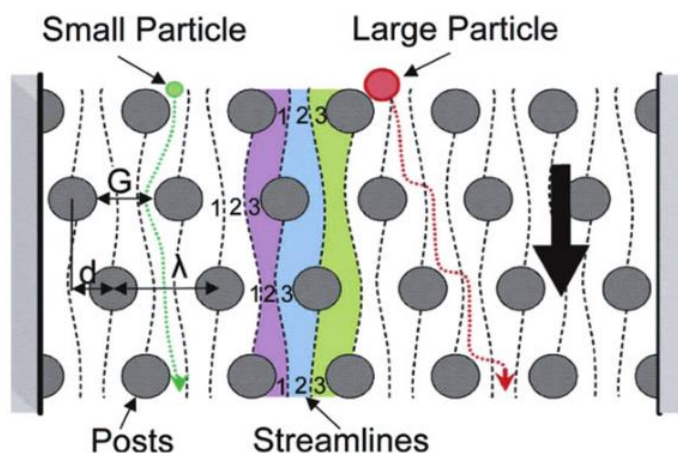


**Figure 1.7:** Deterministic lateral displacement: an array of microposts with a row shift fraction of 1:3 utilized for separation of small particles (green path) and large particles (red path) [20].

Once the particle is larger than the determined critical size, it collides into the obstacle and displaces the particle's trajectory causing a streamline switch. By adjusting the the

gap between obstacles, the obstacle size and the row shift fraction, particles of different diameters can be separated laterally [52, 53]. Deterministic lateral displacement method has been used to sort cells at relatively lower flow rates. Therefore, the length of a device needs to be long enough for efficient sorting.

Inertial hydrodynamic forces acting on cells in a curved microchannel are also other size-based criteria for passive cell sorting (Figure 1.8). The principle behind this approach is Dean-coupled inertial migration. The principle states that the ratio of the net inertial lift force, caused by Poiseuille flow, to the Dean drag force, defined as the centrifugal force, is proportional to the third power of the diameter of a particle in a curved microchannel. The cell separation systems where a form of curvature implemented to the microchannel configuration are named inertial microfluidics. Isolation efficacy of the inertial microfluidic devices has been theoretically related to the size of the target cell and the channel Reynolds number. Therefore, by changing the aspect ratio (height/width) and the flow rate, different size cells can migrate to desired locations transversely and can be subsequently collected at designated outlets with high purity at throughputs in scale of mL/min [10, 54-58].

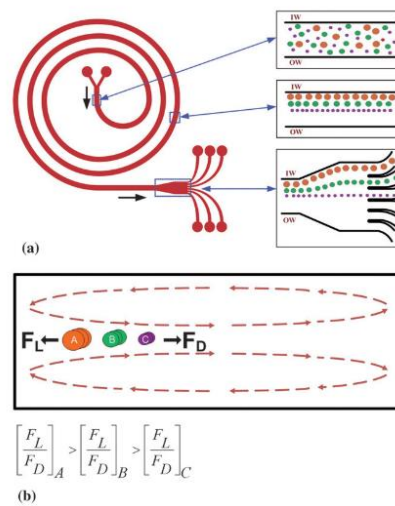


**Figure 1.8:** (a) Schematic of a spiral microchannel based on Dean-coupled inertial migration of different size particles along the channel. (b) Microchannel cross-section illustrating the effect of the ratio of net lift force to Dean drag force ( $F_L/F_D$ ) for particles of different sizes, which determines where particles equilibrate based on their diameters.

As a passive separation method, inertial focusing stands out owing to its simple geometry, easy fabrication, and the capability of qualified cell/particle sorting at high throughput. Spiral microchannels taking the advantage of secondary flows have gained

increasing attention. Secondary flow, also known as Dean flow, is induced at the transverse cross-section of these devices due to the addition of curvature and the consequent drag force so that particles are guided to the corresponding equilibrium positions regarding their size [59, 60]. The curvature is introduced into the systems in several forms such as spiral [10, 54, 57, 61], serpentine [62,63], and curvilinear [58] configurations, as well as expansion–contraction structures [64]. The performance of inertial microfluidic devices is highly dependent on the channel geometry, flow conditions, particle size, and particle concentration. The role of the channel shape in Dean-coupled inertial focusing has been extensively studied in the literature. Many types of channel cross-sections such as square [65], rectangular [10, 54, 61], triangular [66], trapezoidal [67], semicircular [68], and stair-like [69] geometries were investigated. Additionally, the tests with multiple devices working in parallel [70–72] were conducted to further increase the throughput. Some research activities focused on the aspect ratio of microchannels [55, 61, 73]. With the use of the size-dependent hydrodynamic forces, the suspended particles focus into distinctive streamlines along the channel [59, 60] and thus the separation performance could be obtained for particles with different sizes.

However, cell/particle separation methods were explained one by one briefly for the sake of presenting a literature summary, microfluidics mostly include multiple methods integrated in adjacent steps in order to enhance the overall performance.

## **1.2 Unique Aspect**

Inertial microfluidics utilize fluid flow characteristics in micro scale for the focusing and the continuous manipulation of immersed particles. Passive microfluidic technologies do not require any external force. Such technologies take advantage of only hydrodynamic interaction between particles and the fluid. Therefore, it becomes important to master the subject by comprehending the parameters that affect the overall performance of microfluidic systems.

There are numerous aspects to be considered while designing a microfluidic system. These aspects can be listed as throughput, cost, process time and efficiency. Thus, focusing the target particles fast would increase the throughput and herewith decrease the process time and the cost. While equilibrating particles, efficiency must be regarded as well. Because increasing the operation velocity could end up weakening

the separation yield. In the light of these explanations, regular spiral devices have been modified geometrically to improve the overall performance. Spiral microchannels already were studied and promising outcomes have been reported so far [10, 54, 56, 61, 80]. Main design parameter that are influential in the focusing behavior of immersed particles in a curved channel are explained earlier. However, there are very limited number of studies in literature about the effects of the curvature radius on this field of study. As novelty, there were two different modifications applied into the geometry of a spiral microchannel.

First one is conversion of Archimedean spiral form into an ellipse shape. In such elliptic spiral microchannels, the governing drag force gains more strength compared to the case of a regular spiral microchannel. The underlying reason for that is the effect of a curvilinearly increasing curvature radius that leads particles to entrain laterally faster without defocusing. In the proposed devices, the magnitude of the lateral velocity varies due to the change in the channel curvature. Yet, this change is not as sudden as in serpentine and curvilinear channels. Moreover, the direction of the rotation does not change. Due to the alternating curvature, the drag force either increases or decreases along each quarter loop and this is where they differ from regular spiral channels having an ever-decreasing drag force, which is a key element of particle focusing in curved microchannels. Therefore, the elliptic configurations make particles migrate quicker to the equilibrium positions than spiral channels with the help of the changing curvature. Since the lateral velocity profile is not distributed as much as in serpentine channels, the particles also preserve their focusing. As elliptic channels enable faster focusing to equilibrium positions, the total length requirement would be shorter than spiral channels and accordingly the fabrication and operational costs and the footprint area would be lower. Hence, these configurations could lead to an outstanding separation performance.

Along with the elliptic microchannels, a regular spiral channel with microposts was developed as well. As mentioned earlier, hydrodynamic flow fractionation method that acts in spiral channels already manage particles to align at certain positions along the channel width based on their size. By positioning single row of microposts as in the deterministic lateral displacement method, additional clog-free filtration process was aimed to apply on the particles before separation. The microfiltration unit was implemented right before the collection outlets in order to enhance the separation

efficiency. Due to issues faced during the fabrication of the microposts, the study was pursued with only elliptic microchannels, which eventually exhibited promising performance.

### **1.3 Research Structure and Thesis Outline**

Four types of devices differing by the initial aspect ratio of elliptic geometry were designed and fabricated. The theoretical flow patterns were compared with the numerical simulations of laminar flow in the microchannels. Then, the proposed devices were tested with 10 and 20  $\mu\text{m}$  fluorescent particles at different channel Reynolds numbers to determine the optimum flow rates, at which the best particle separation could be achieved. The study was carried out with fluorescently dyed polystyrene microspheres representing blood cells and CTCs due to the unavailability of live cells and the corresponding equipment and facilities. Later, extensive tests were conducted to assess particle migration and the overall separation yield. The proposed microdevices will have the potential to be used and further developed for routine monitoring of cancer progression and guiding cancer therapeutics in clinical settings.

## 2. THEORY

At first, Segré and Silberberg [74] in the early 60's observed immersed particles migrating laterally towards to certain equilibrium positions in a laminar flow. At that time, the underlying reason that explains how such behavior occurred was nontrivial. Later on, it was understood that the phenomenon could be explained by previously unknown forces acting on particles during an inertial flow. By understanding the principles behind, a variety of microfluidic technologies has been proposed for particle manipulation and separation so far. These technologies are categorized as label-free and biochemical applications including separation, isolation and enrichment of targeted micro-particles or cells. There are two types of applications as active and passive depending on whether any external force is applied or not. Among active methods, flow velocity is generally limited, which allows the manipulative forces to effectively overcome the drag forces. Since the speed is low, creeping flow (Stokes regime) dominates and inertial effects are neglected compared to viscous forces occurring in active microfluidics. On the other hand, passive technologies relying on ordinary hydrodynamic forces have relatively simpler configurations and higher flow rates. As the throughput of the system increases, Reynolds number converges to a laminar-turbulent transition region of confined flows. Hence, fluid inertia is no more negligible.

One of the trending passive technologies is inertial microfluidics since its first use [63]. Due to high throughput, less complex structure and precise manipulation, the use of purely hydrodynamic interactions has emerged during the last decades. While approaching turbulent regimes, both fluid inertia and viscosity play their roles on the foundation of inertial microfluidic technology. Through straight channels, immersed particles in a suspension migrate axially at their equilibrium positions under the influence of several inertial effects. The inertial migration phenomenon has been established by the interaction of two inertial effects; the shear gradient lift force  $F_s$ , due to the parabolic velocity profile causing particles move away from the centre of the channel, and the wall lift force  $F_w$ , caused by the squeezed fluid between the suspending particle and the adjacent walls, which is exerted on the particle towards the

centre [75]. The inertial balance positions of particles are reported around 0.6 times of the channel radius to the channel centreline in a circular channel [74]. In rectangular channels, four equilibrium positions occur upon each channel wall [59].

Once a form of curvature is introduced in channel design, or flow in a straight channel is disturbed by a mechanism, secondary flow realizes because of a pressure gradient formed in the radial direction. This results in the fluid in the centre gaining more momentum than the fluid near the walls [60]. Following that the fluid elements around the channel centreline is pushed outwards and drive relatively stagnant fluid elements near the walls inwards. This movement creates two counter-rotating streams, called Dean vortices along the circumference [75]. With the help of secondary flow effect, the number of equilibrium positions reduces from four to one in the curved rectangular channels as shown in Figure 2.1. In this regard, size-dependent focusing of suspended particles according to the ratio of inertial lift force and Dean flow drag force perpendicular to the stream ( $F_L/F_D$ ) promises manipulation of the inertial equilibrium positions in order to obtain high purity separation without requiring any additional force field.

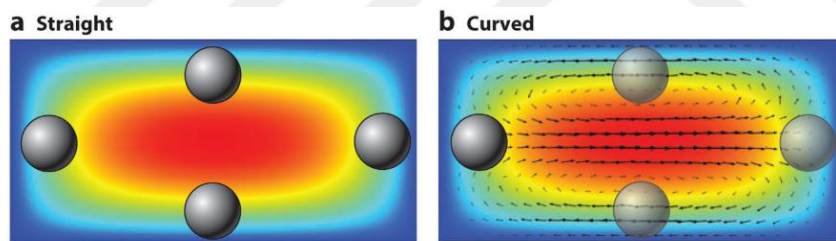


**Figure 2.1:** (a) Equilibrium positions in straight channels. b) Single equilibrium position (near the wall closer to the curvature center) in curved channels and the black vectors represents Dean vortices (secondary flow) [59].

## 2.1 Dynamics Forces Acting on a Migrating Particle in Inertial Microfluidics

### 2.1.1 Net inertial lift force

There are four lift forces laterally acting on a neutrally buoyant particle flowing in a Poiseuille flow through a straight channel,: Wall-induced lift force formed by the disturbance of the flow field between particles and the channel wall, shear gradient lift force as a result of the curvature of the parabolic fluid velocity profile, Magnus force due to slip-rotation and Saffman force due to slip-shear [75]. For lateral migration of particles, Magnus force and Saffman force are mostly recognized as negligible

compared to the shear gradient lift force directing particles toward the walls, and wall-induced lift force leading particles toward the centre of channel [76]. Also diffusion effect is mostly neglected in the analysis of inertial microfluidics since Péclet number is high and consequently convection dominates over diffusion in the transport [75]. Due to the counteraction of shear gradient lift force and wall-induced lift force (Figure 2.2), particles migrate along various equilibrium positions where these lift forces balance each other and this theory can explain the preceding observation of Segre and Silberberg mentioned previously [74].

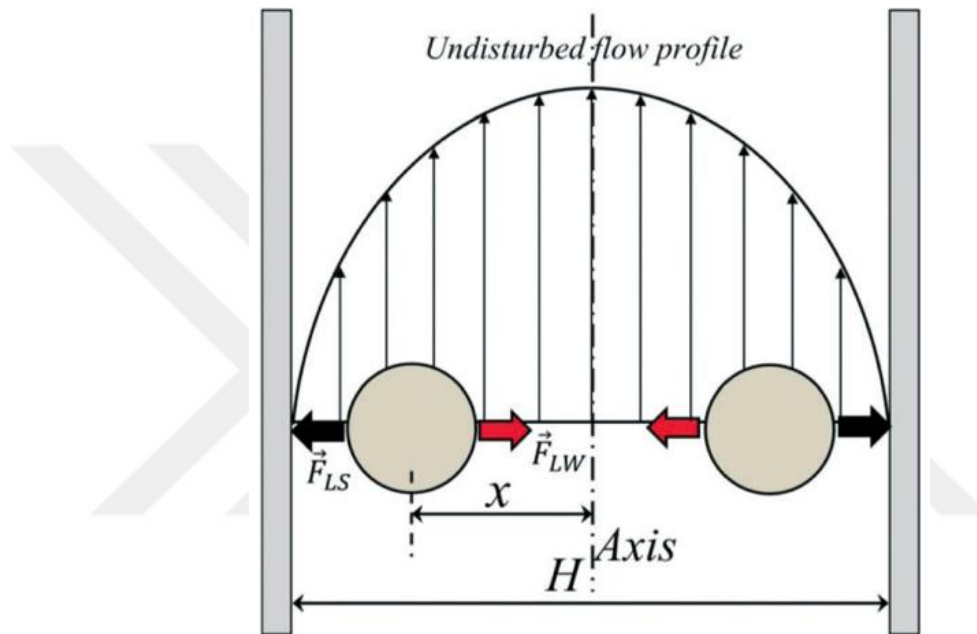


**Figure 2.2:** Shear gradient (black) and wall-induced (red) lift forces acting on particles [75].

### 2.1.1.1 Wall-induced lift force

As mentioned above, the existence of a wall causes two effects; immersed particles moving slightly slower than the fluid and pressure building up in the contraction region between the particle and the walls of a channel. Hence, generated lift force repels particles to direct away from the walls. Boundaries slow down the motion of the particle due to the no-slip condition at the walls when the main flow direction is both parallel and perpendicular to the wall. Besides, the wall exerts lift force directing perpendicularly to the main flow direction when particles are moving parallel to the boundary (Figure 2.3).

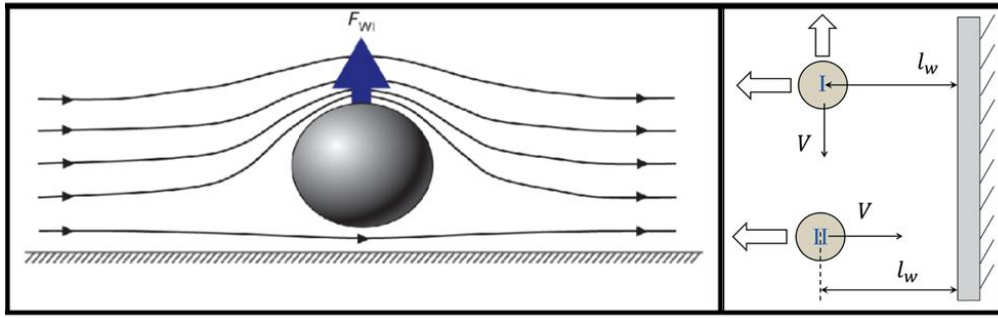


**Figure 2.3:** Wall-induced lift force [59, 75].

### 2.1.1.2 Shear gradient lift force

A particle experiences different relative velocity magnitudes on either side because of parabolic velocity profile in a channel. Thus, the fluid flow around the particle generates a shear gradient lift force in order to balance the difference in relative velocity over the particle (Figure 2.4). This force is similar to the Saffman force, yet it is in the higher relative velocity direction as pressure is lower near the wall side. The shear-gradient lift force leads particles migrating toward the walls while the wall lift force performs contrarily [77].

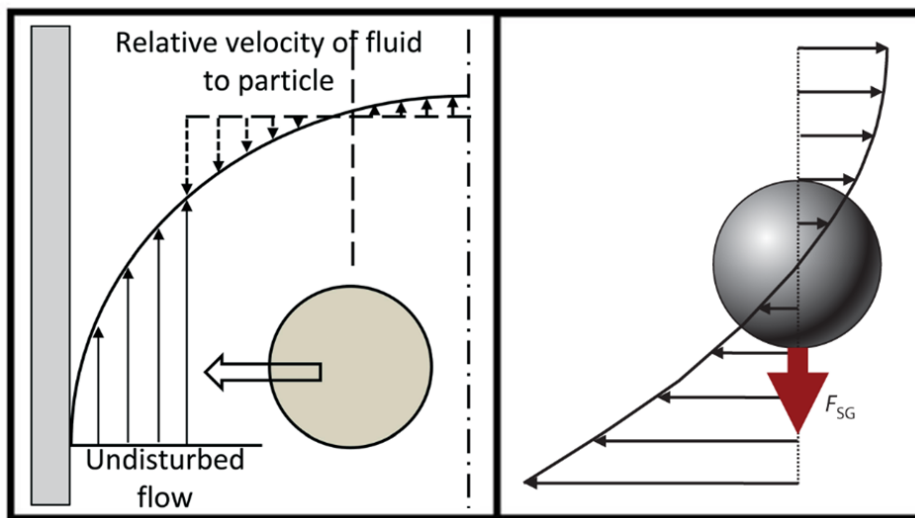


**Figure 2.4:** Shear gradient lift force [59, 75].

### 2.1.2 Viscous drag force

A drag force arises in need of removing the fluid elements out of the way of the moving particle. In general, two constituents of viscous drag force form. First, the relative axial velocity of a particle generates drag lengthwise (Figure 2.5). In addition, secondary flow induced by the curvature of the channel or structural disturbance results in

secondary drag force, so called Dean drag force. Dean flow allows size-based separation by exploiting the dependence of the drag force on particle size [75]. The ratio of the drag force and the net lift force scales with third power of particle diameter. In curved microchannels, the Dean drag force and the net lift force are opposed to each other only near the inner wall, which constitutes the basis of inertial focusing.

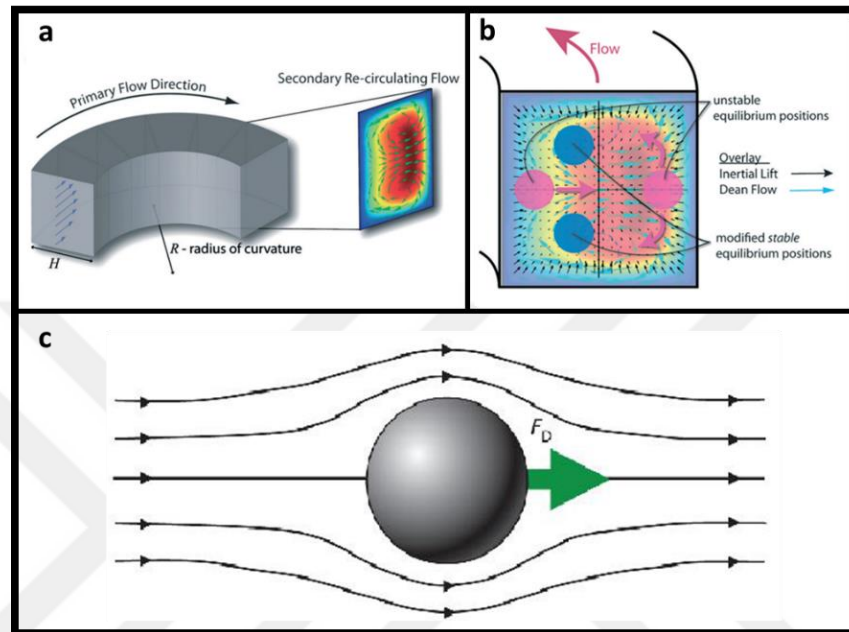


**Figure 2.5:** a) Dean Flow in a rectangular channel, b) equilibrium position due to Dean flow effects, c) Drag force acting on a suspended particle [59].

### 2.1.3 Deformability-induced lift force

In inertial microfluidics, additional lift force occurs in case of non-rigid particles such as blood cells flowing in a microchannel. This force is called deformability-induced lift force acting perpendicularly to the main streamline. Because of the interaction of this force, it was reported that the inertial equilibrium line occurs closer to the centerline when compared to the results for non-deformable particles [78]. This force has significant usage in CTC separation applications. For the case of polystyrene particles, which are non-deformable, deformability-induced lift force was eliminated.

## 2.2 Design Principle

The acting forces on microparticles suspended in a base fluid determine their equilibrium positions. In microchannels with a rectangular cross-section, the inertial lift forces including shear gradient lift force ( $F_S$ ) and wall induced lift force ( $F_W$ ) are

the dominant forces. The parabolic velocity profile stems from Poiseuille flow inside the microchannel and makes microparticles move from the centerline region toward the channel wall by causing the shear gradient lift force. The rotational wake around the particle disappears or an asymmetric wake is generated with a decrease in the distance between microparticles and walls. As a result, a lift force, known as the wall induced lift force, directed away from walls toward the channel center appears [59, 79]. Accordingly, these lift forces make the particles to position across the microchannel cross-section at locations, where these forces balance each other so that the focusing positions of particles are established. The net inertial lift force ( $F_L$ ) resulting from these forces is expressed as:

$$F_L = C_L \frac{\rho U_{max}^2 a_p^4}{D_h^2} \quad (2.1)$$

where  $\rho$  is the fluid density,  $U_{max}$  is the maximum fluid velocity,  $a_p$  is the microparticle diameter, and  $D_h$  is the hydraulic diameter of the channel.  $C_L$  is the lift coefficient, which is dependent on the particle position and fluid velocity [59,79]. The magnitude of the lift coefficient is zero at the center of the channel and varies between 0.2 and 0.5 in microfluidics applications [58, 80].

Because of curvature addition to the microchannel, secondary flows occur creating two counter-rotating vortices known as Dean vortices, which lead to the Dean drag force (Figure 2.6). The following equation includes the Dean drag force, where  $\mu$  and  $U_{De}$  represent the fluid viscosity and Dean velocity, respectively [10]:

$$F_D = 3\pi\mu U_{De} a_p \quad (2.2)$$

where  $U_{De}$  is calculated by using the following correlation [81]:

$$U_{De} = 1.8 \times 10^{-4} De^{1.63} \quad (2.3)$$

where  $De$  is defined as the dimensionless Dean number and is given as follows:

$$De = \frac{\rho U_f D_h}{\mu} \sqrt{\frac{D_h}{2R}} = Re_c \sqrt{\frac{D_h}{2R}} \quad (2.4)$$

$$Re_c = \frac{\rho U_m D_h}{\mu}, \quad (2.5)$$

where  $R$  is the curvature radius,  $U_m$  is the mean fluid velocity, and  $Re_C$  represents the channel Reynolds number.

The direction of the secondary flow is toward the outer wall around the channel centerline, while the flow recirculates toward the inside wall along the top and bottom regions of the channels, which results in the Dean drag force ( $F_D$ ) acting on the microparticles as demonstrated in Figure 2.6. This force emerges due to the centrifugal acceleration, which moves the fluid at the center faster than the fluid near the top and bottom walls and thus the secondary flow formation redistributes the velocity profile and reduces the equilibrium positions of suspended particles to a single one near the inner wall (Figure 2.1).

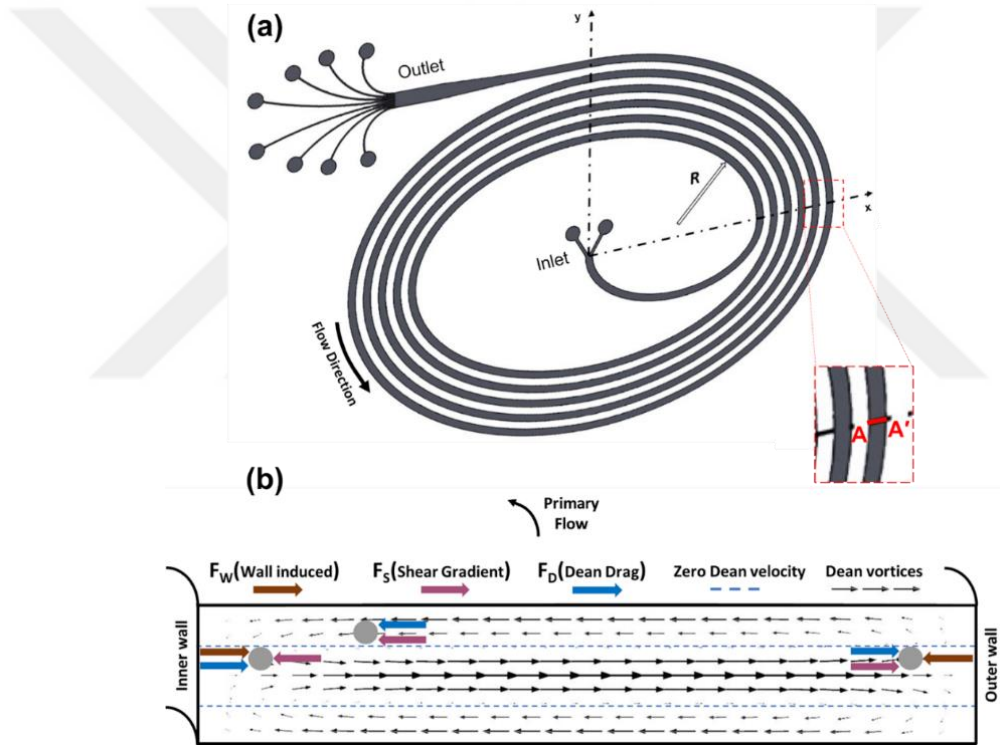


**Figure 2.6:** (a) Schematic of an elliptic spiral microchannel shown in a Cartesian plane including radius of curvature,  $R$  at a random position and the location of A-A' cross-section. (b) A close-up view of A-A' plane illustrating secondary flow induced

Dean vortices, zero Dean velocity lines and a force diagram demonstrating the directions of wall induced lift force ( $F_W$ ), shear gradient lift force ( $F_S$ ) and Dean drag force ( $F_D$ ) acting on a particle at various locations.

The Dean drag force and the net inertial lift force manipulate the trajectory of particles in microchannels. Neutrally buoyant particles circulate in two symmetric counter-rotating vortices induced by the pressure difference due to the secondary flow. Near the outer wall,  $F_L$  and  $F_D$  are in the same direction, and the particles follow the Dean

vortices regardless of their size. The particles moving at the top and bottom halves of the microchannel are strongly assisted by lateral Dean flows to migrate to the inward direction. However, the net lift force and Dean drag force on particles act in opposite directions near the inner wall. Regarding the magnitude of these forces, particles will either equilibrate or continue to entrain in the Dean vortex. The ratio of the inertial lift force to the Dean drag force is directly proportional to the third power of the particle diameter ( $F_L/F_D \propto a_p^3$ ) and determines the equilibrium position of the particles. The lift forces dominate by pushing particles to an equilibrium position when  $F_L/F_D$  is equal to 1 or greater [56]. When this ratio goes to zero, Dean drag force dominates and the particles unbalance their inertial equilibrium and remain entrained within the secondary flow streamlines.

### 2.3 Design of the Microchannels

Passive inertial microfluidic devices operate under flow conditions between the creeping flow and the turbulent flow. Thus, both inertial and viscous effects can not be ignored. A variety of phenomena occurs while sorting particles in spiral microchannels under the combined effects of lift and drag forces. Thus, a parameter space is required to be defined before the design. There are two dimensionless numbers should be addressed initially. Firstly, Reynolds number (Eq. 2.5). is the main parameter in any type of fluidic systems. Additionally, the governing phenomenon in Dean-coupled inertial migration applications is the secondary flow formation entraining the particles and balancing the inertial lift forces. The strength of the secondary flow induced in the radial plane is characterized by a key parameter, Dean number (Eq. 2.4). Therefore, another parameter that should be addressed is Dean number. Dean number is a dimensionless number and a function of the channel Reynolds number, the channel hydraulic diameter, and the curvature of radius (Eq. 2.4). Hence, secondary drag force occurs proportional to the magnitude of Dean number. These non-dimensional numbers are used generally for presenting the experimental findings.

Beside these non-dimensional numbers, fluid properties (density, viscosity) are also effective parameters. Water, which is a Newtonian fluid, was used as a working medium. In addition to the fluid properties, flow conditions (flow rate, pressure, body forces) are important and can be phrased as operational parameters. Body forces are

neglected in passive microfluidic devices. Since plain water was employed in the experiments under normal conditions, only flow rate has been investigated in this study.

The lift coefficient, which is determinant in focusing dynamics of particles in such systems, should also be addressed. Lift coefficient depends on the Reynolds number, the particle size, the channel cross-section and the position of the particle. The effects of the lift coefficient dependence on these parameters has not been covered within the context of this work due to the fact that forces acting on particles are not calculated or measured.

Other parameters worth mentioning are the experimental parameters such as particle diameter and particle concentration. The study was carried out with fluorescently dyed polystyrene microspheres representing blood cells and CTCs due to the unavailability of live cells and the corresponding equipment and facilities. The dilution concentration of particles in suspension was determined to be lower than 0.01 v/v% (volume/volume) for the sake of eliminating particle interactions and avoiding the alteration of the fluid properties.

Moreover, the geometrical design parameters are also utilized for characterization of focusing patterns in the confined flows. These parameters can be listed as the width, the height, the length and the radius of curvature. The channels were decided to have a rectangular cross-section considering the ease of manufacturing and the available equipment. In addition, the channel cross-sectional dimensions were fixed for all channels. The channel length required for particles to focus varies with the employed flow rate. Therefore, the length was determined long enough to provide applicability within wider range of flow rate. Among abovementioned design parameters, the radius of curvature stands out as one of the least focused parameter compared to all. Thus, the manipulation of flow conditions by playing with the curvature radius has been studied.

In this study, four spiral microchannels with elliptic configurations and a regular spiral channels with microfiltration units implemented were designed for investigation. The elliptic spiral microchannels differing by their elliptic aspect ratio are defined as Case1, Case 2, Case 3 and Case 4 in order to provide a clearer explanation. Here, the elliptic aspect ratio is expressed as the ratio of ellipse size in the horizontal axis to the

vertical axis. In addition, Case 5 indicates the regular spiral channels with microfiltration unit consisting of a row of microposts. With the establishment of novel microchannels, there are new parameters rising with respect to the geometrical modifications applied to the channels. For elliptic channels (Case1-4), the aspect ratio of ellipse shape should be considered as key parameter. Therefore, differing elliptic aspect ratios were introduced for investigation. For Case 5, the micropost shape and size, the gap between posts and the array angle are governing parameters in determination of critical particle size for filtration process.

Finally, the channel design steps were explained in the following section.

### 2.3.1 Cross-sectional shape

The ratio of particle diameter to the hydraulic diameter ( $a_p/D_h$ ) is reported as a significant parameter for inertial particle migration, and particles can equilibrate across the cross-section of channel due to the effect of Dean flow enabling particles to focus at single streams for  $a_p/D_h \geq 0.07$  [59, 80]. Yet, equilibration in rectangular microchannels depends on the shorter channel dimension, which is the channel height ( $H$ ), rather than  $D_h$  because of shear rate variations across the channel cross-section [10]. Below this value, focusing may get weaker, even disappear [63,79,80]. In the light of the limitation explained above, maximum hydraulic diameters for equilibrated suspension of different size particles are listed in Table 2.1.

**Table 2.1:** Maximum channel heights based on the particle size for successful focusing.

Particle Diameter, $a_p$ ( $\mu\text{m}$ )	Maximum Channel Height, $H$ ( $\mu\text{m}$ )
5	71.4
10	142.9
15	214.3
20	285.7

For experimental study, particles with a diameter of 10  $\mu\text{m}$  and 20  $\mu\text{m}$  are selected. Thus, it is determined that the channel height should be under 142.9  $\mu\text{m}$ . On the other hand, it is not allowed to construct a microchannel higher than 100  $\mu\text{m}$  because of microfabrication equipment restraint. In the light of the criterion of  $a_p/H \geq 0.07$  and the abovementioned fabrication limits, 500- $\mu\text{m}$  wide and 90- $\mu\text{m}$  high microchannels (Aspect Ratio: 0.18) were determined. In addition, two inlets and eight outlets

including the prior widened section was designed for sample circulation through the device.

### 2.3.2 Curvature radius

In spiral microchannels, curvature radius is one of the most important features. It affects Dean Number and therefore drag force acting on suspended particles. The addition of curvature to a microchannel path creates secondary Dean flow which is generated due to the velocity distribution across the cross-section [82-84]. Due to the parabolic velocity profile, the fluid elements closer to the centerline have larger inertia as the velocity is maximum and relocate quicker than fluid near the walls. Regarding conservation laws, the centrifugal effect creates a pressure gradient on the radial axis and subsequently relatively stagnant fluid near the walls recirculates inward, finally forming two symmetric circulating vortices. The intensity of the secondary flow in a curved channel is characterized by the non-dimensional Dean number ( $De$ ). Dean number basically depends on the hydraulic diameter, the channel Reynolds number and the curvature radius (Eq. 2.4).

When  $De > 20$ , drag from Dean vortices is larger than the inertial lift forces for most particle sizes and disturbs particle focusing and results in particle mixing [63]. Additionally, Reynolds number converges laminar-turbulent transition region of confined flows. Hence, fluid inertia is no more negligible, as the throughput of the system increases. Considering the limitation of  $De < 20$ , the Table 2.2 including geometrical parameters for each design is introduced.

**Table 2.2:** The common geometrical parameters and initial geometrical parameters of the first loop for the design of all cases.

		Initial Geometrical Parameters					
Channel Height ( $\mu\text{m}$ )	Channel Width ( $\mu\text{m}$ )	$r_x$ (mm)	$r_y$ (mm)	Initial Aspect Ratio (IRA)	Maximum Radius of Curvature, $R_{\text{max}}$ (mm)*	Minimum Radius of Curvature, $R_{\text{min}}$ (mm)**	
Case 1		12	8	3:2	18.0	5.3	
Case 2		11	9	11:9	13.4	7.4	
Case 3	90	500	9	11	9:11	13.4	7.4
Case 4			8	12	2:3	18.0	5.3
Case 5			10	10	1:1	-	-

\* $R_{\text{max}} = \max(r_x^2/r_y, r_y^2/r_x)$  and \*\* $R_{\text{min}} = \min(r_x^2/r_y, r_y^2/r_x)$

In a regular spiral channel, the center of the curvature is the same at any point, and the radius increases linearly throughout the microchannel. However, in ellipse-shaped spiral channels, the center of the curvature changes, thereby making the radius of the curvature change along the channel. As a result, the channel curvature radius increases in a curvilinear rising trend. The elliptic design redistributes the intensity of Dean vortices enabling the focusing patterns to form quickly. Moreover, the outlet radius of the curvature for each case differs due to the elliptic configuration. Dean number decreases with the increasing radius of curvature at the exit, as the channel shape approaches to the horizontal geometry (Case 1 and 2). Contrarily, smaller curvature radius at the exit results in greater  $De$  (Case 3 and 4).

It is also worth noting that Case 1 and Case 4 have similar geometrical features and therefore similar fluid flow characteristics as well as Case 2 and Case 3. The only difference lies in the channel orientation. For instance, the wider part of the microchannel is located in the x-axis for Case 1, whereas the wider part is in the y-axis for Case 4. Even though they have similar shapes, Cases 1 and 2 differ from Case 3 and Case 4 in terms of the final quarter loop configuration, which leads to increasing or decreasing curvature radius before the channel outlet. Therefore, this phenomenon will be investigated along with the effect of changing radius of curvature.

### 2.3.3 Channel length

Next, volumetric flow rate should be specified by considering fully developed laminar flow in the channel. Microfluidic devices function at a flow rate between 50  $\mu\text{L}/\text{min}$  - 10mL/min in literature [85, 86]. On the other hand, most of the researchers apply flow rates mostly in the range of 0.1-1.0 mL/min [55, 67]. Thus, the volumetric flow rates in the range of 0.5-3.5 mL/min were determined to examine for separation of 10  $\mu\text{m}$  and 20  $\mu\text{m}$  particles.

In addition to the channel width, the channel length is another parameter to be investigated. From Asmolov's lift force equation [87] with Stokes drag assumption, the expression for particle lateral migration velocity is expressed as [80]:

$$U_L = \frac{\rho U_{max}^2 a_p^3 C_L}{3\pi\mu D_h^2} \quad (2.6)$$

where  $\rho$  is the fluid density,  $\mu$  is the fluid viscosity,  $U_{max}$  is the maximum fluid velocity,  $a_p$  is the microparticle diameter,  $D_h$  is the hydraulic diameter of the channel,

and  $C_L$  is the lift coefficient. The total channel length required for particles to focus completely at the equilibrium positions is given as:

$$L_I = \frac{U_m}{U_L} \times L_M \quad (2.7)$$

where  $U_m$  is the fluid mean velocity and  $L_M$  is the migration length. Similarly, the channel length required for Dean migration is given as [80]:

$$L_D = \frac{U_m}{U_{De}} \times L_M \quad (2.8)$$

Using the above equations, the maximum required length for the current work can be calculated as approximately 20 cm. Subsequently, a five-loop spiral design with 500  $\mu\text{m}$  spacing between two consecutive loops was considered for sorting 10  $\mu\text{m}$  and 20  $\mu\text{m}$  particles. Therefore, the length of the microchannels was approximately 43 cm and the current configurations are effective within the range of 0.5 mL/min- 3.5 mL/min.

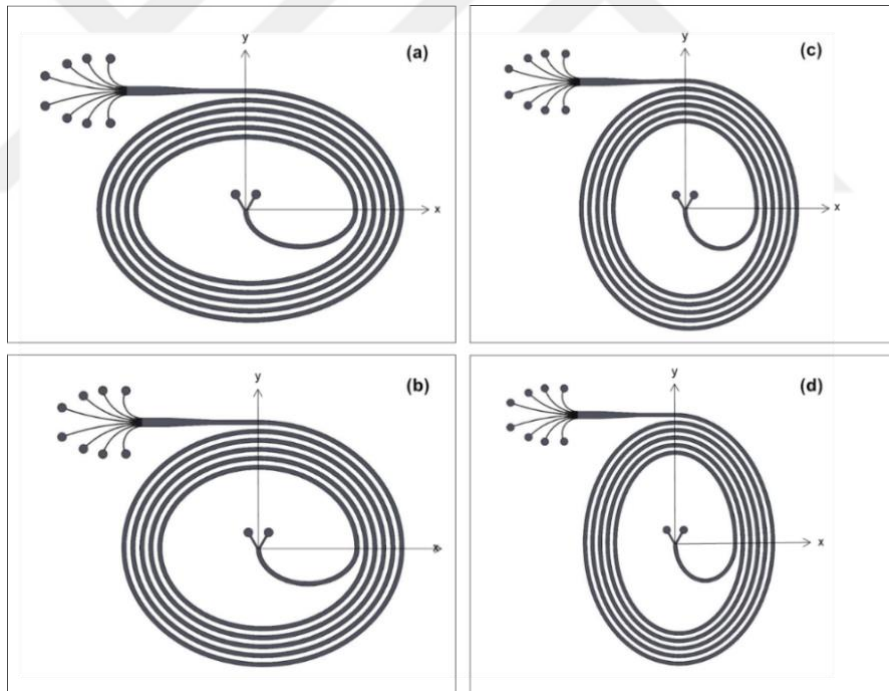


**Figure 2.7:** Schematics of the Elliptic Spiral Microchannels: (a) Case 1 (Initial Aspect Ratio ( $IAR$ ): 3:2), (b) Case 2 ( $IAR$ : 11:9), (c) Case 3 ( $IAR$ : 9:11) and (d) Case 4 ( $IAR$ : 2:3).

The distance between two consecutive loops was kept the same as the channel width. As a novel aspect, elliptic configuration was incorporated in the channel geometry. The proposed elliptic channels have an initial aspect ratio ( $IAR$ ) of 3:2, 11:9, 9:11 and

2:3 as seen in Figure 2.7. Once the elliptic geometry is introduced as the channel geometry, the intensity of Dean vortices alternates due to the change in centrifugal effects. Hence, the configuration becomes more effective in terms of enhancing the focusing capability. The resultant Dean numbers of each of the elliptic channels are shown in Figure 2.8.

In the Cartesian coordinates as shown in Figure 2.6(a),  $r_x$  and  $r_y$  representing the radii of the microchannels on both x and y axes are tabulated in Table 2.2. Regarding the geometrical parameters of an ellipse, maximum and minimum curvature radii were calculated using the corresponding formulas (Table 2.2). For Cases 1 and 2 (Figure 2.7(a) and (b)), the maximum curvature radius is located in y-axis. However, the maximum radius moves to the x-axis in the remaining cases (Figure 2.7(c) and (d)). Moreover, the curvature radius at the end of the curved section of the microchannel changes for each case. Case 1 has the largest radius of curvature at the exit, while the radius of curvature in Case 4 is smaller than the rest (Table 2.2).

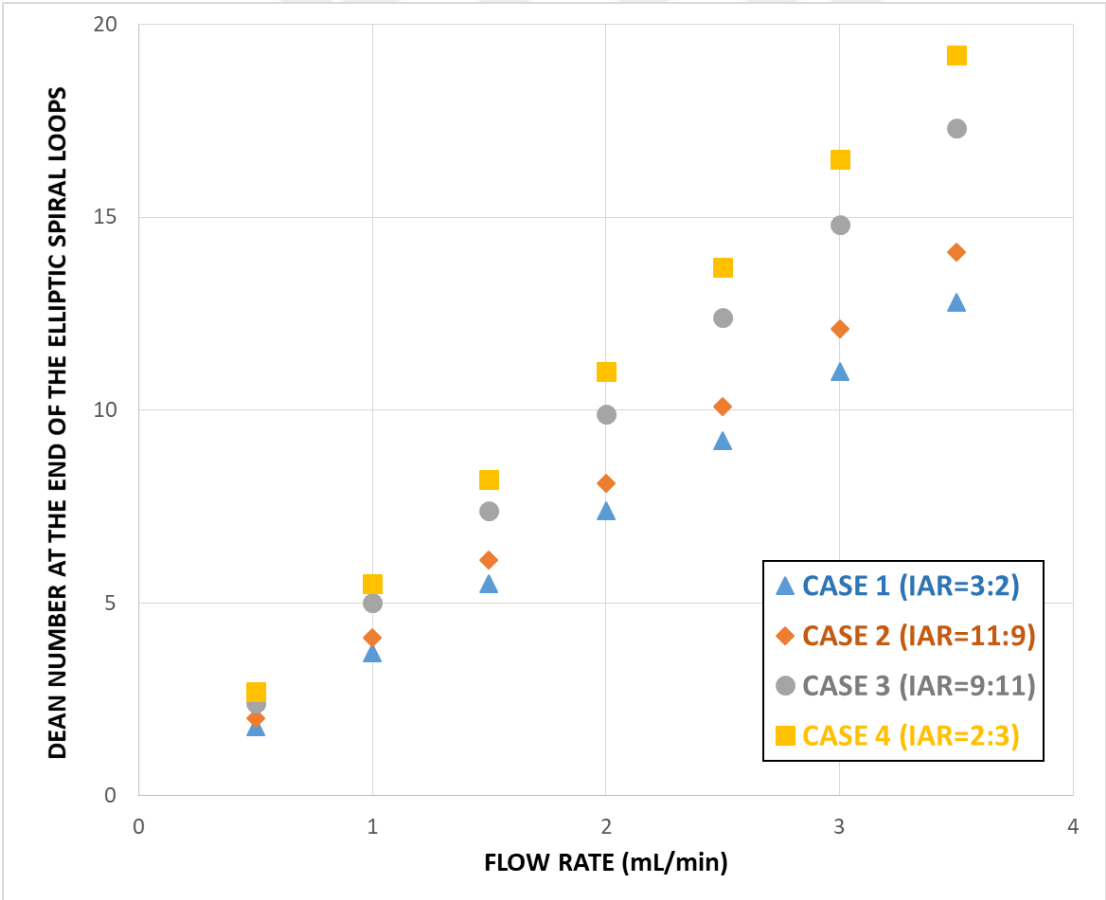


**Figure 2.8:** Dean number variations at the end of the curved section of the elliptic spiral microchannels.

From Eq. 2.4, it can be seen that Dean number is inversely proportional with the curvature radius. Thus, increasing radius results in decreasing Dean number, and herewith secondary flow induced drag effect. The effect of curvature radius in Case 1-4 was demonstrated in Figure 2.8. In the figure, Dean number at the end of the elliptic spiral loops are derived for varying flow rates. Even though, the same flow rate is applied, Dean number alternates for each case.

### **2.3.4 Microfiltration design**

Due to the fact that tumor cells tend to have larger size than that of constituent blood cells, numerous microfluidic systems have been developed to isolate larger cells by means of filtration based on their size. In such size-based filtration devices proposed in literature [6,24,30,49], the spacings between microbarriers (e.g. microposts, microdams) allow the smaller blood cells to pass through, while inherently larger and stiffer CTCs might be captured. Such designs suffer from clogging by captured cells. A particle-sorting platform was developed by integrating two approaches; size-based filtration and Dean flow fractionation. By combining the strengths of these two methods, a self-design device that functions continuously in a label-free and clog-free manner is expected to be accomplished. Hence, by adjusting design parameters and observing their overall contributions, an acceptable degree of separation purity is aimed by preventing clogging due to accumulation of cells.

At the end of a spiral microchannel with initial curvature radius of 1 cm (Table 2.2), several cylindrical microposts are designed to be placed with a certain gap of 40  $\mu\text{m}$  in between (Figure 2.9). In order to achieve more precise separation, this microfiltration platform is expected not to allow targeted 20  $\mu\text{m}$  particles pass through the barriers into the outlet recruited for 10  $\mu\text{m}$  particles. Various micropost diameters from 30  $\mu\text{m}$  to 90  $\mu\text{m}$  were considered for investigations. Moreover, the array angle of microposts, also known as row shift fraction, was assigned as 0.10 (1:10). Depending on experimental outcomes, main parameters of the microposts such as diameter, shape, gap and row shift fraction may be changed accordingly.

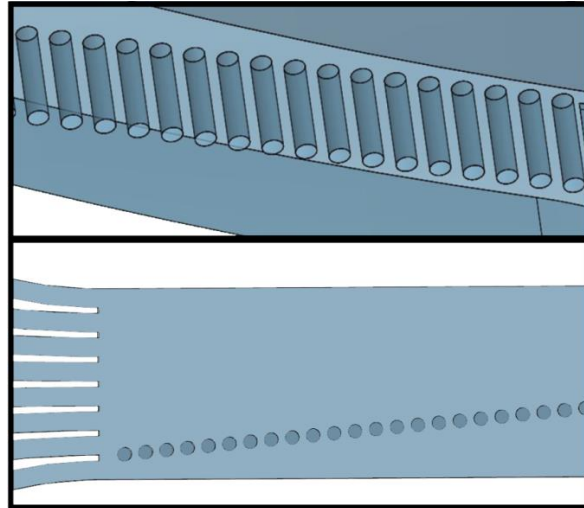


**Figure 2.9:** Microfiltration platform implemented in Case 5 where the diameter of the microposts is  $60\ \mu\text{m}$  and the gap is  $40\ \mu\text{m}$  with row shift fraction of 1:10.

Finally, the design step of the microfluidic devices was completed and the study proceeded to the fabrication and experimental investigation stage.

### 3. EXPERIMENTAL METHODS AND DATA ANALYSIS

#### 3.1 Device Fabrication

The standard soft lithography method was used to fabricate the PDMS (polydimethylsiloxane) microchannels. Here, the device fabrication protocol is described in detail.

##### 3.1.1 Substrate (SU-8 mold) preparation

###### 3.1.1.1 Cleaning of the wafers

3” silicon (Si) wafers (University Wafer, Inc.) were cleaned in order to receive a good adhesion of SU-8. The wafers were bathed in Isopropyl alcohol (IPA). Then they were dried by  $N_2$  gas before moisture removal at the hot plate ( $\sim 110^\circ\text{C}$ ).

###### 3.1.1.2 Spin coating of SU-8

SU-8 3050 (Microchem Corp.) is an epoxy-based, negative photoresist material, thus UV light (ultraviolet light) exposure enhardens the material and makes it insoluble in a developer. After cleaning, the photoresist was spun at gradually increasing speed (Table 3.1) to the desired thickness of approximately  $90\ \mu\text{m}$  via a spin coater (Dorutek).

**Table 3.1:** Speed settings for spin coater.

# of step	Time	Rotational speed	Acceleration
1	7 second	500 rpm	200 rpm/sec
2	30 second	1750 rpm	200 rpm/sec

As the spinner (Figure 3.1) exerts centrifugal force, pouring SU-8 precisely at the center of the wafer is crucially important. Following the coating step, Si-wafer was soft baked on the  $95^\circ\text{C}$  hot plate for 15 minutes in order to ensure mechanical stability and smoother adhesion between wafer and SU-8 photoresist.



**Figure 3.1:** Spin Coater with the control panel.

### 3.1.1.3 UV light exposure

Once the layout of the microchannel is determined, acetate photomasks were designed and printed (Çözüm Baskı Merkezi, Ankara) accordingly. In order to perform exposure perfectly, the channel pattern should be fully transparent. Therefore, the photomasks, where the channel pattern is transparent and the rest is opaque, were published in acetate. The acetate masks (Figure3.2) used in the lithography were produced by high-resolution printing (3600 DPI).

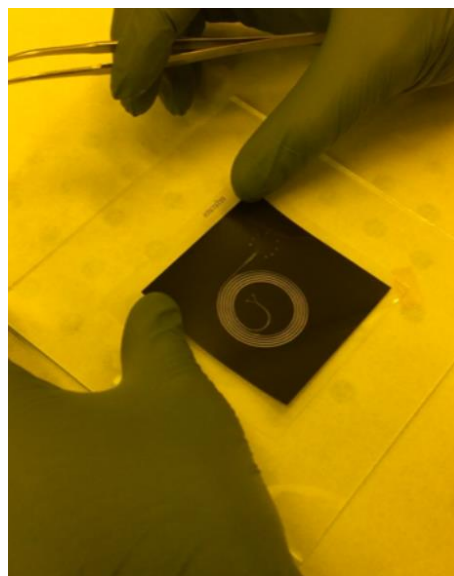


**Figure 3.2:** Acetate Photomask.

Following the spin coating, the coated Si-wafer was exposed to UV light using a Mask Aligner UV-Lithography device (Midas System Co., Ltd., MDA-60MS Mask Aligner 4”) (Figure 3.3) through the image reversal photomasks printed on acetate. Hence, the regions of the SU-8 not facing UV light dissolved in the development process, while the exposed regions remained hard due to the fact that SU-8 is a negative photoresist.

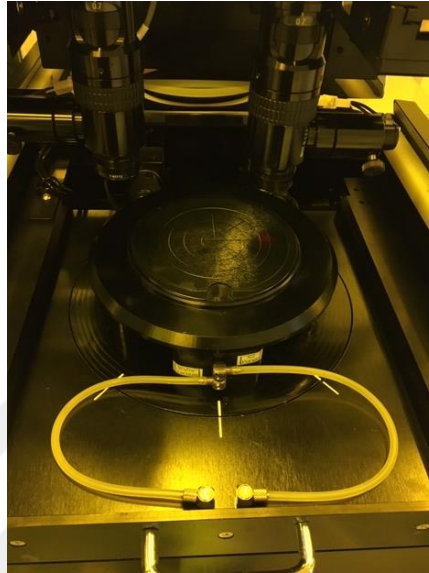


**Figure 3.3:** Mask Aligner 4”.

SU-8 coated wafer was put under the UV light exposure via a Mask Aligner UV-Lithography device. The purpose of the UV light exposure is to initiate the cross-link in the photoresist. The cross-linkage affects the properties of the resin and SU-8 becomes hard. The exposure time/dose (Table 3.2) depends on the microchannel thickness. The photoresist-coated wafer was put on UV light for 12 seconds to accomplish the 90- $\mu\text{m}$  channel height.

**Table 3.2:** Exposure Input Data for the Mask Aligner.

Time	12 sec
Energy	283.2 mJ
Power	23.6 mW

#### 3.1.1.4 SU-8 development

After exposure, the wafer is rested for a while. Then the post-exposure baking on the hot plate takes place to create thermal, physical and chemical stability. It is baked on a 95°C hot plate for 5 minutes right after soft baking at 65°C for 1 minute.

The fabrication of the SU-8 mold was concluded with the development, where the unexposed area was removed in the SU-8 Developer (Microchem Corp). Even though development time depends on the given durations in the SU-8 3000 datasheet, eye inspection is critical to visually follow cleaning of the unexposed SU-8 from the surface and prevent the mold from overdevelopment. Although 7-15 minute of development is suggested by the producer, it has been observed that developing for 6-7 minutes was sufficient for the proposed devices.

As a final touch, the developed wafer was rinsed with additional SU-8 developer and isopropyl alcohol in given order and then dried with  $N_2$  gas. Finally, the designed microchannel was revealed on the substrate and thus the SU-8 mold or PDMS replica is fabricated.

Prior to PDMS casting, SU-8 mold was checked visually under a microscope. Then the desired channel height was measured with a Surface Profiler (KLA Tensor). Figure 3.4 illustrated the channel height distribution along the channel width.

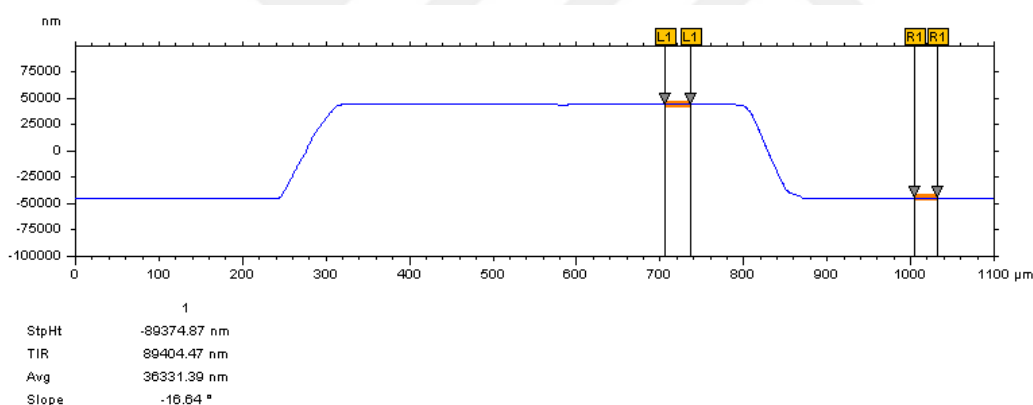


**Figure 3.4:** An example of a microchannel surface profile (Case 1).

### 3.1.2 Microchannel fabrication

#### 3.1.2.1 PDMS casting

PDMS (polydimethylsiloxane) is commonly used elastomeric polymer in fabrication of microfluidic devices. PDMS is nontoxic and transparent and has a low viscosity. In addition, it has the ability to be cured at low temperatures, which makes it greatly functional in soft lithography. As PDMS is highly flexible, it is easy to peel off from the mold (Figure 3.5) without any harm.

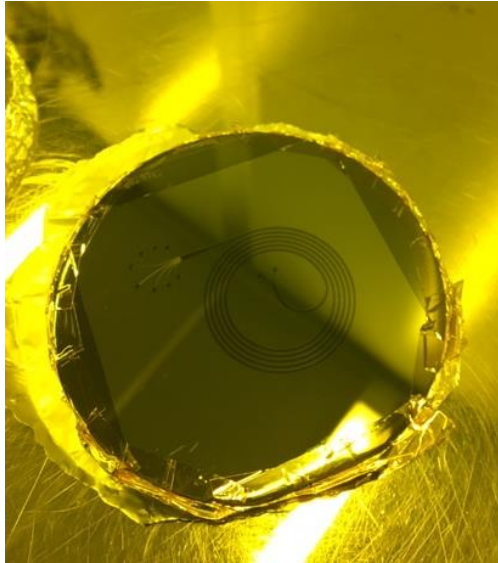


**Figure 3.5:** SU-8 Mold ready for PDMS Casting.

In PDMS casting protocol, the first step is covering a glass petri dish with aluminum foil to be able to tape the SU-8 mold onto the foil. By taping, PDMS leakage is aimed to be prevented. A PDMS prepolymer base and curing agent (Sylgard 184 silicone elastomer kit, Dow Corning) were mixed at a 10:1 ratio in a plastic dish and stirred for at least a few minutes and poured over the SU-8 master mold firmly placed in a glass petri dish coated with aluminum foil. For a single microfluidic device, approximately 30 gr of prepolymer and 3 gr of curing agent were used. Dispensing the material at the center of the substrate from a low altitude is critical considering the risk of air bubble formation. Thus, the PDMS mixture was carefully casted over the mold, then degassed for half an hour before curing at 75 °C for 3 h in a vacuum oven (Sheldon Manufacturing, Inc.) (Figure 3.6).



**Figure 3.6:** Degassing in the vacuum oven.

Following the curing and cooling down, the baked PDMS was detached carefully by releasing first all the borders, continuing towards the centre, and peeled off the remaining parts (Figure 3.7).

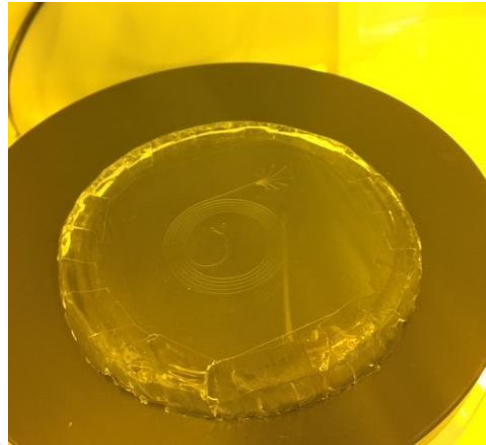


**Figure 3.7:** PDMS cast after baking and removing from the SU-8 mold.

Later, the part where the channel configuration locates was cut with a scalpel and inlet and outlet holes were punched using a 21-gauge needle with sharpened tips (Figure 3.8).

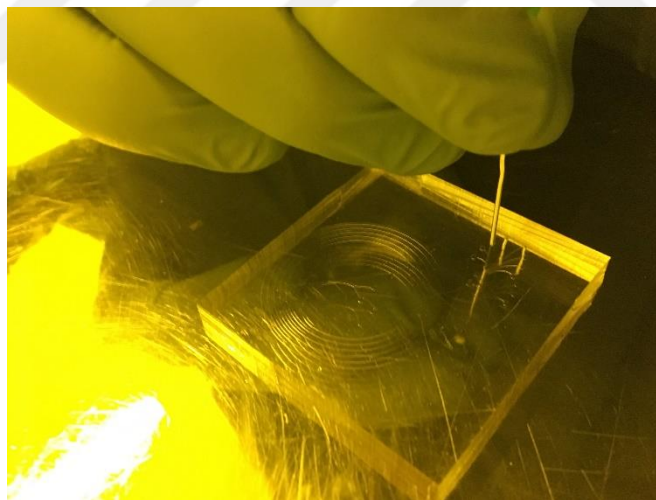


**Figure 3.8:** Punching the inlet and outlet holes on PDMS.

### 3.1.2.2 $O_2$ Plasma Treatment

PDMS is hydrophobic, thus an additional process,  $O_2$  plasma treatment, is required to modify the surface in order to achieve adhesion on other objects. Before the treatment, both the PDMS channels and 1-mm-thick microscope glass slides were cleaned off dust and debris with isopropyl alcohol and deionized water, dried with  $N_2$  gas and rested on a hot plate. A Plasma Cleaner is the most commonly used tool to bond the

PDMS. After cleaning, surfaces of the glass slide and PDMS channel were activated in an oxygen plasma device (Harrick Plasma Cleaner) (Figure 3.9).



**Figure 3.9:** Harrick Plasma Cleaner.

In the plasma cleaner, the surfaces of the PDMS channel and glass slide were activated by being exposed to  $O_2$  plasma. Both parts were placed on a large glass petri dish while the bonding surfaces are facing up. The flow rate of oxygen gas was set by the PlasmaFlo gas flow mixer precisely (Figure 3.10) and the chamber of plasma cleaner is fed oxygen where the manometer is set at 3 mbar.



**Figure 3.10:** Gas Flow Mixer (PlasmaFlo).

Then the oxygen feeding is cut by turning the valve off and the system was vacuumed by a pump until the pressure inside goes below 500 mTorr. Once the desired pressure was reached, the power was turned on by rotating the RF (Radio Frequency) switch to

the high level. It is critical to observe glowing purple color through the chamber window as seen in Figure 3.11.

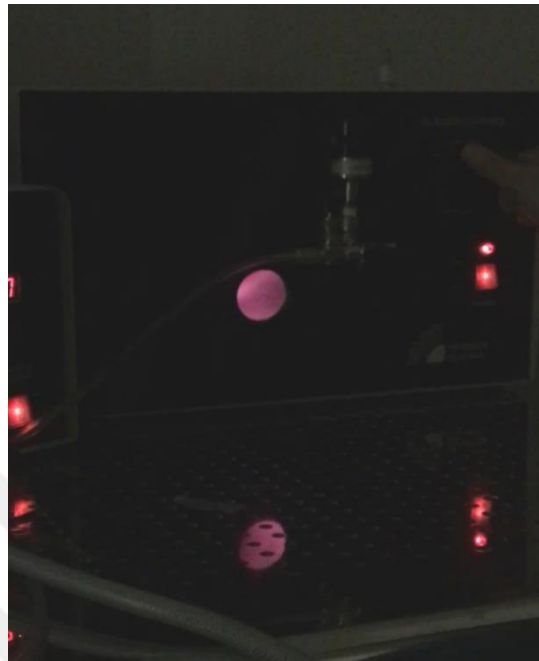


**Figure 3.11:** Purple glow during oxygen plasma treatment.

Subsequently, the oxygen-feeding valve was opened for less than a millisecond and closed again. Since the inner pressure rose, this step was repeated when the pressure is back to under 500 mTorr. After 60 seconds of intermittent  $O_2$  injections, both the RF switch and vacuum pump were turned off. The PDMS microchannel and the glass slide were evacuated immediately. Finally, the enclosed microchannel configurations were formed by rapidly pressing the treated surfaces to achieve permanent bonding. Hot plate treatment at 70°C for 15 minutes was applied to enhance the bonding, if necessary.

### **3.1.2.3 Fabrication issues of microfiltration unit of Case 5**

#### Poor resolution of photomask

Due to the deficiency of printing resolution, relatively small features in the photomasks such as microposts do not appear as proper as they are sketched (Figure 3.12). Yet, the shape of the microposts are not foreseen to have an effect on their functionality of filtration. Using the current photomasks, the microchannel production has been carried on. The results will be discussed in the following sections.

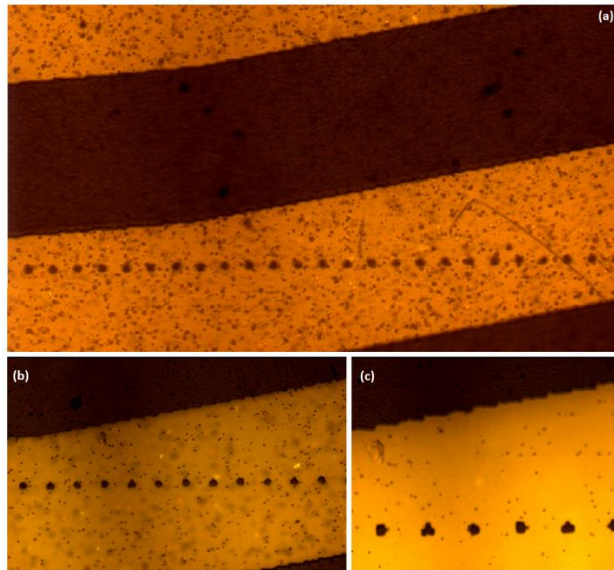


**Figure 3.12:** Microscopic images of the photomask of the microfiltration unit of 30  $\mu\text{m}$  posts under (a) 5x, (b) 10x, (c) 20x zoom.

*Fabrication problems of microposts*

As mentioned above, the quality of the photomasks, especially in the microfiltration part, is not as desired. Although the fact that the microposts are not perfectly round is not critical in terms of the functionality, their rigidity is crucial for the sake of well bonding between posts and the microscope slide which is placed at the top part of the microchannel. Because of currently unknown reasons, the SU-8 mold of the microfiltration unit has been built as in Figure 3.13.

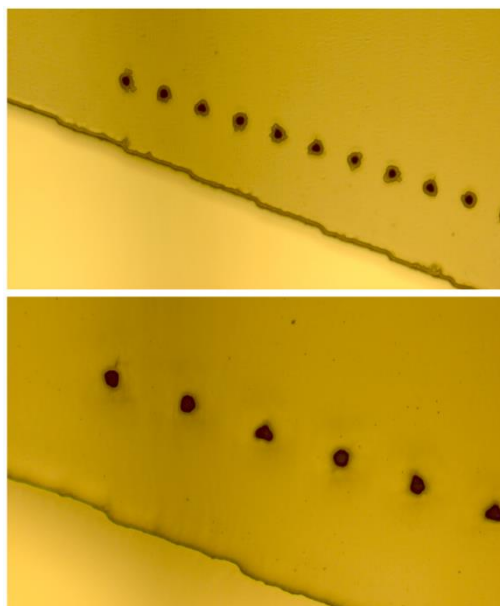


**Figure 3.13:** Microscopic images of the SU-8 mold of the microfiltration unit consisting of 30  $\mu\text{m}$  posts under 10x and 20x zoom.

As shown in the Figure 3.13, the holes, which are supposed to be utilized in manufacturing the microposts by casting PDMS, should be as bright as the lower parts. The holes being dark indicates that non-exposed SU-8 could not be developed properly due to the small geometrical features. By using the mold shown in the Figure3.13, a microchannel consisting of microposts with supposedly 30  $\mu\text{m}$  width and 90  $\mu\text{m}$  height has been manufactured (Figure 3.14). As it can be observed from the microscopic view, both the shape and the stiffness of the posts are problematic. It is estimated that the imperfections of the SU-8 mold resulted in non-rigid microposts that are also narrower and shorter than the design.

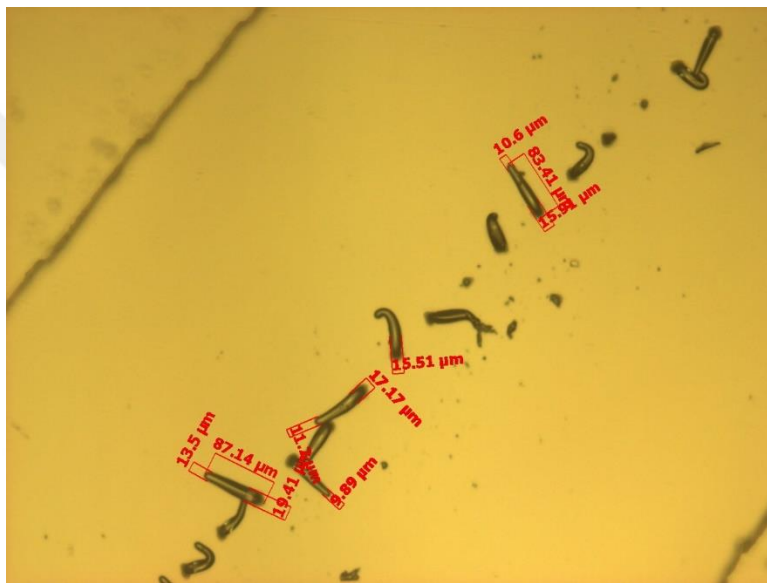


**Figure 3.14:** Microscopic image of the microfiltration unit made of PDMS consisting of 30 $\mu\text{m}$ -wide and 90 $\mu\text{m}$ -high posts under 20x zoom with dimensioning.

Because of poor photomask quality for smaller features, it seems hard to manufacture microposts properly. In order to eliminate this problem, the design was updated by widening the micropost diameter to 60 and 90  $\mu\text{m}$ , which is more likely to provide better quality. By using the reprinted photomasks, Case 5 with 60- $\mu\text{m}$  wide microposts were fabricated. In the development stage, it was observed that SU-8 could not be fully removed from some of the micropost pores (Figure 3.15). Thus, this will result in shorter microposts. Henceforth  $O_2$  bonding will not be succeeded at locations where the micropost height fell short and this condition will cause rigidity problems during experiments especially at higher flow rates.

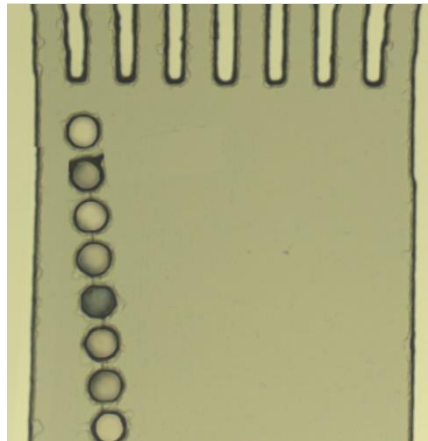


**Figure 3.15:** Underdevelopment issue in Case 5 with 60- $\mu\text{m}$  wide microposts.

For 90- $\mu\text{m}$  wide microposts, development outcome was successful. Even though the microposts were fabricated rightly with a round shape as designed, this time the problems were rupture of the microposts and clogging as demonstrated in Figure 3.16. While removing the cast PDMS out of the mold, some of the microposts were lost due to the rupture. The broken microposts remained in the mold and were not ejectable. Therefore, it was not possible to reuse the SU-8 mold. In case of successful demolding, the clogging occurred during the primary tests because of PDMS debris and dust particulate. Thus, the investigation of the microfiltration implemented spiral device was suspended as a future work.

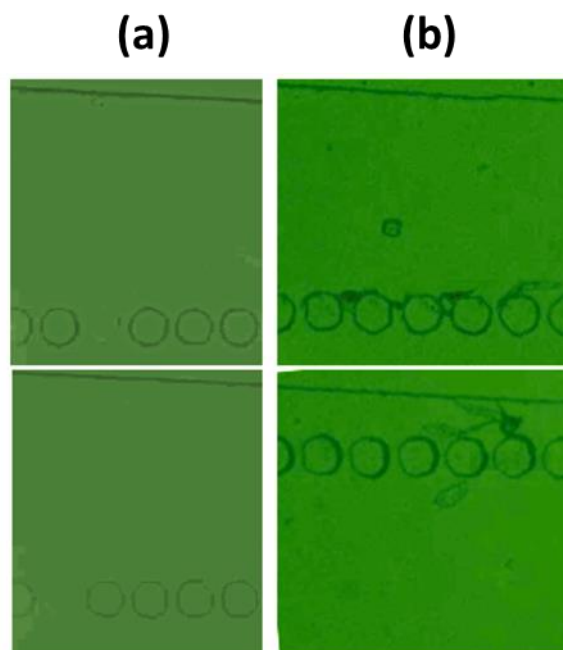


**Figure 3.16:** (a) The rupture of microposts and (b) the clogging in Case 5 with 90- $\mu\text{m}$  wide microposts.

### 3.2 Suspension Preparation

Fluorescently dyed polystyrene microspheres with diameters of 10  $\mu\text{m}$  (Invitrogen, Crimson), and 20  $\mu\text{m}$  (Fluoresbrite, Yellow-Green) were used in this size-based separation study. As a medium, deionized (DI) water was utilized to dilute the samples. The dilution concentration of particles in suspension was determined to be lower than 0.01 v/v % (volume/volume) for the sake of eliminating particle interactions. The particle suspensions were prepared separately for each size with the help of a magnetic stirring bar in a glass bottle and were loaded to a plastic syringe. Microparticle suspensions were injected through the devices via a syringe pump (Cole-Parmer).

### 3.3 Experimental Setup

The experimental setup was built as in Figure 3.17. The sample of fluorescent polystyrene particles suspended in DI water was injected into the elliptic spiral microchannels through a single inlet using a Cole Parmer syringe pump.

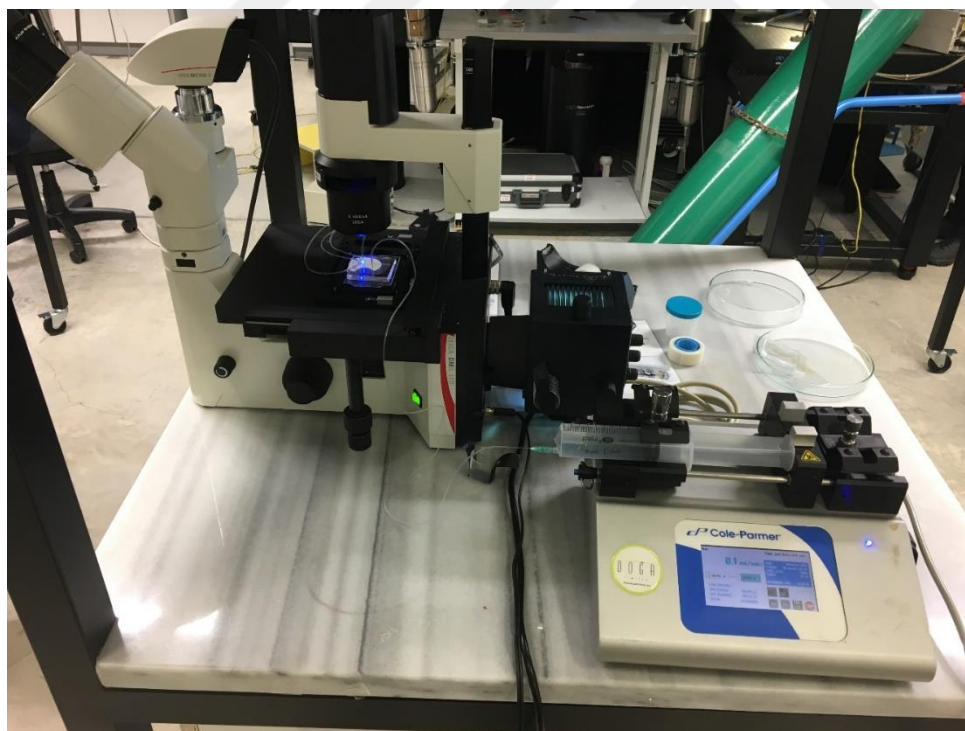


**Figure 3.17:** Experimental Setup.

Even though two inlets were originally considered in the design, only one inlet was utilized for the current study. The suspension of each particle was pumped into the system at flow rates varying from 0.5 to 3.5 mL/min, which were precisely set by the

control unit of the syringe pump. Moreover, a solution containing both 10  $\mu\text{m}$  and 20  $\mu\text{m}$  diameter polystyrene particles was used to check for the compatibility of the results from individual tests. For connection between inlet and outlet openings to the device, TYGON tubing with an internal diameter of 250  $\mu\text{m}$  (LMT-55, IDEX Corp.) and corresponding fittings (IDEX Corp.) were utilized (Figure 3.18).

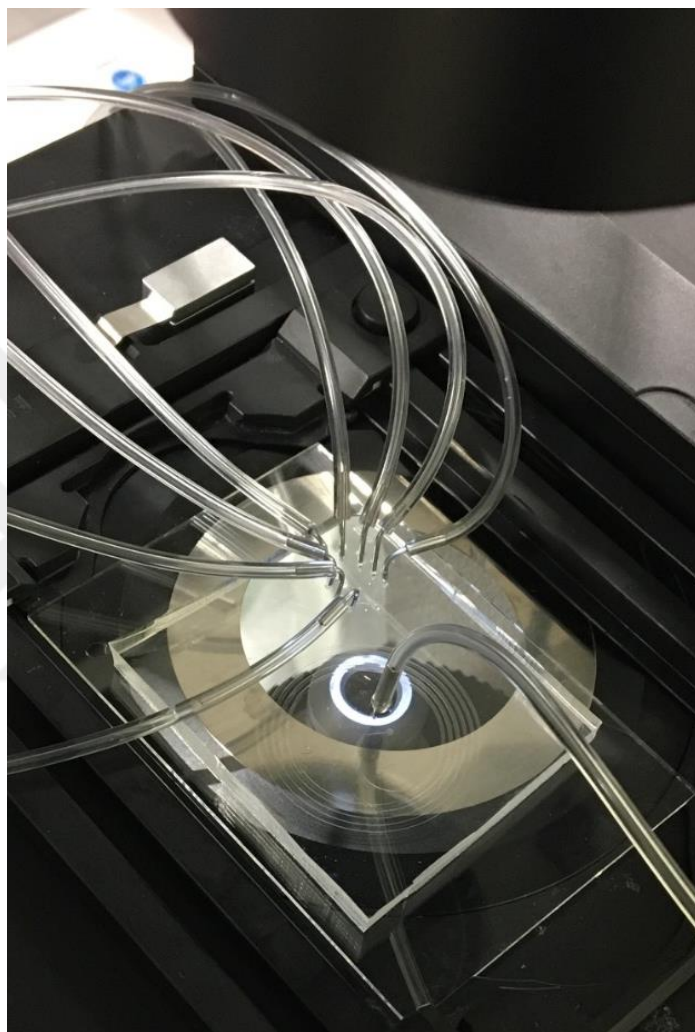


**Figure 3.18:** Connection of single inlet and 8 outlet openings with corresponding tubings and fittings.

Both videos and image sequences were captured in the expanded outlet section via an inverted phase contrast microscope (Olympus IX72) (equipped with a (12-bit) charge) coupled with a device camera (Olympus DP 72), mercury lamp (Olympus U-LH100HG), and Olympus software (cellSens Imaging Software). The particle migration trajectories were recorded by employing filter cubes of the microscope depending on the dye color of microspheres at exposure time of 600 ms at each flow rate for each case. By injecting a suspension of 10  $\mu\text{m}$  and 20  $\mu\text{m}$  particles, the samples

isolated from each outlet were collected into separate small tubes in order to count the number of particles and thus deduce particle separation capability. The counting was done visually by using the inverted phase contrast microscope.

### 3.4 Data Analysis

Along with Olympus software (cellSens), ImageJ (Fiji) software was used for post processing. By analyzing the recorded fluorescent videos, flow fractionation and particle migration were observed at each flow rate. By applying the modules of ImageJ software, the focusing positions and width of focused streamlines for each particle size were determined by stacking discrete frames retrieved from the relevant videos and by investigating the intensity profile across the channel width. Then, the superimposed image of both particles was created by ImageJ software to visualize the capability of multi-particle separation.

### 3.5 Numerical Simulations

The COMSOL Multiphysics finite element software program (COMSOL Inc., Stockholm, Sweden) was utilized to simulate Newtonian fluid flows in the four proposed elliptic microchannel configurations with a rectangular cross-section ( $500 \mu\text{m} \times 90 \mu\text{m}$ ).

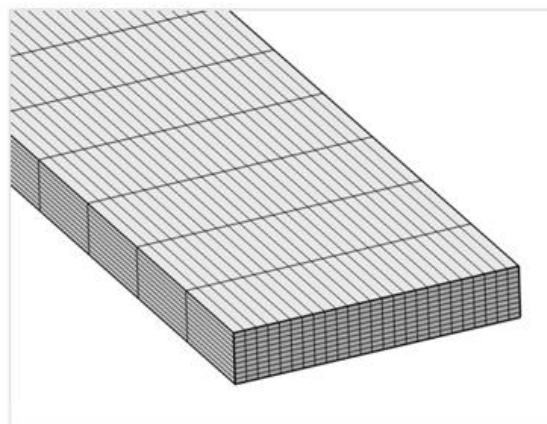


**Figure 3.19:** Uniform hexahedral mesh used in numerical simulations.

These channels were modeled by importing the 3D CAD drawings built in SolidWorks software. The geometries were simplified by reducing the number of inlets and outlets to one for each. Following that, a computational domain was created using mapped

meshes, which were refined until the number of elements was ensuring the accuracy of results. Then the mapped network was swept through the entire geometry in order to finalize the meshing step. After that, numerical simulations were done with the computational domain consisting of uniform hexahedral mesh (Figure 3.19) with more than 450,000 elements and an average quality of approximately 0.92.

Since the working medium was deionized water in the experiments, the required physical properties (density and viscosity) for water were acquired from the library of the commercial software. The laminar flow module was selected to calculate the 3-D flow field in rectangular microchannels considering the range of employed Reynolds numbers in this study. Later initial and boundary conditions were defined for laminar flow modelling. Normal inflow velocity was derived by using Equation 2.5 and applied as the inlet condition. For the outlet, gauge pressure was set to 0 Pa. At walls, no-slip condition was assigned as boundary condition. All of the initial values were determined as zero. Finally the computational model was developed.

Each model was solved using the GMRES iterative solver to simulate a single-phase, incompressible, and steady laminar flow governed by the continuity equation (Equation 3.1) and the Navier–Stokes equations (Equation 3.2) expressed as:

$$\nabla \cdot (u) = 0 \quad (3.1)$$

$$\rho(u \cdot \nabla)u = \nabla \cdot [-pI + \mu(\nabla u + (\nabla u)^T)] \quad (3.2)$$

where the symbols were defined as default in COMSOL. ( $u$ , velocity field and  $p$ , pressure)

The numerical study was performed for all the microchannels with elliptic configurations in order to predict the focusing behavior of the particles. The flow velocity within the cross-section (secondary Dean flow) were extracted and demonstrated by using arrows. The length and thickness of the arrows were proportional to the magnitude of the velocity. Therefore, insights about the flow field in the experimental study could be provided by obtaining Dean vortices in the transverse direction regarding the primary flow. Thus, the numerical results serve for supporting the theoretical conceptualization, predicting the experimental findings and further discussing the effects of velocity distribution on the focusing behavior and trajectory of the particles.

It is worth noting that the lateral velocity induced by secondary flow is only one component of focusing dynamics. Thus, numerical simulations of fluid flow was utilized to make a rough estimation about possible experimental outcomes. In addition, there is a small simulation error since the effect of the occupied volume of the particles in the fluid were not taken into consideration. For these reasons, the computational study was not beneficial to validate of experimental results.



## 4. RESULTS AND DISCUSSION

### 4.1 Laminar Flow Simulation

#### 4.1.1 Secondary flow analysis along the microchannels

A computational study was performed in order to understand the underlying fluid flow in the microchannel configurations. Figure 4.1 demonstrates the variation of tangential velocity vectors over the colored velocity profile of the primary flow at six different positions from the most inner loop to the last one for Case 1. These positions are labeled accordingly in Figure 4.1(a). Figure 4.1(b) shows the cross-sectional velocity distribution provided at each cross-section (numbered in Figure 4.1(a), respectively). Accordingly, the Dean vortices in the first loop ( $De = 22.5$ ) are more intense and then gradually lose their intensity until the exit of the channel ( $De = 16.5$ ) as expected due to the nature of spiral configuration regarding the increasing spiral curvature and decreasing Dean number.

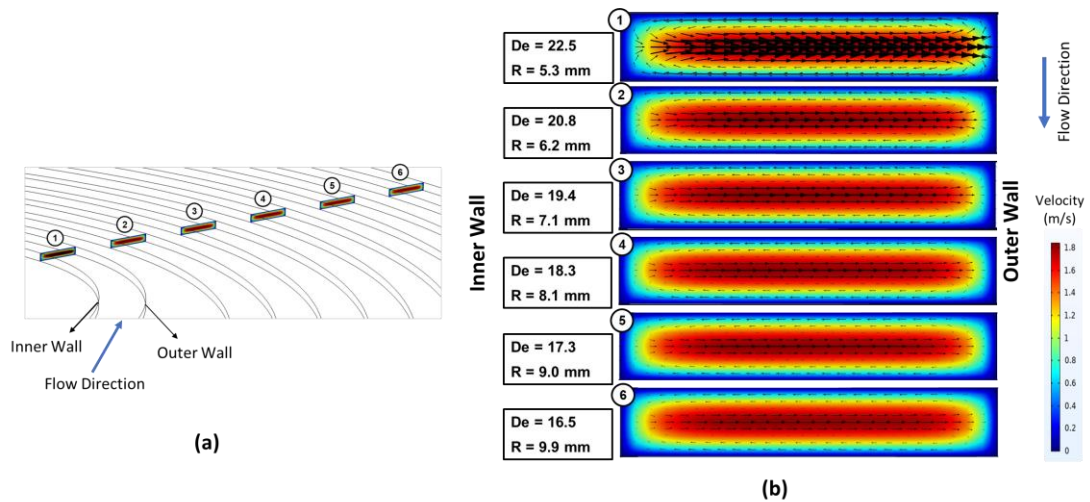


**Figure 4.1:** (a) Six different cut-plane positions labeled starting from the inner loop along the primary flow direction, and (b) a closer look at the vectoral variation of lateral velocity distributions over the colored velocity profile of the primary flow at six different cross sections throughout the channel. The cross-sectional velocity profiles were retrieved from COMSOL Multiphysics simulation results of Case 1 (IAR=3:2) at the volumetric flow rate of 3 mL/min.

#### 4.1.2 The effect of alterations in the radius of curvature

Since the microchannels have elliptic configurations, the position of the curvature center varies resulting in the alterations in radius of curvature. Figure 4.2 illustrates the lateral velocity vectors occurring in the flow rate of 3mL/min for all four cases at the beginning and at the end of the last quadrant loop of the channels. The largest Dean velocity can be observed in Figure 4.2(a) and (h), where the radius of curvature is the smallest with 9.9 mm. In Case 1 (Figure 2.7(a)), the curvature radius increases throughout the last quarter loop of the channel from 9.9 mm to 22.2 mm and hence the Dean vortices become smaller (from Figure 4.2(a) to 4.2(b)) and drops from 16.5 to 11.0. This explanation is also valid for Case 4 (Figure 2.7(d)) in the exact opposite way. In Case 4, the minimum curvature radius occurs at the exit leading to a higher lateral velocity (Figure 4.2(h)). For Case 2 and Case 3 (Figure 2.7(b) and (c)), the curvature radius changes within a relatively narrow range (between 12.3 mm and 18.3 mm). Thus, the magnitude of the counter-rotating vortices does not vary drastically along the last  $\frac{1}{4}$  loop prior to the exit. As Dean number alternates between 12.1 and 14.8, the intensities of Dean vortices are rather low.

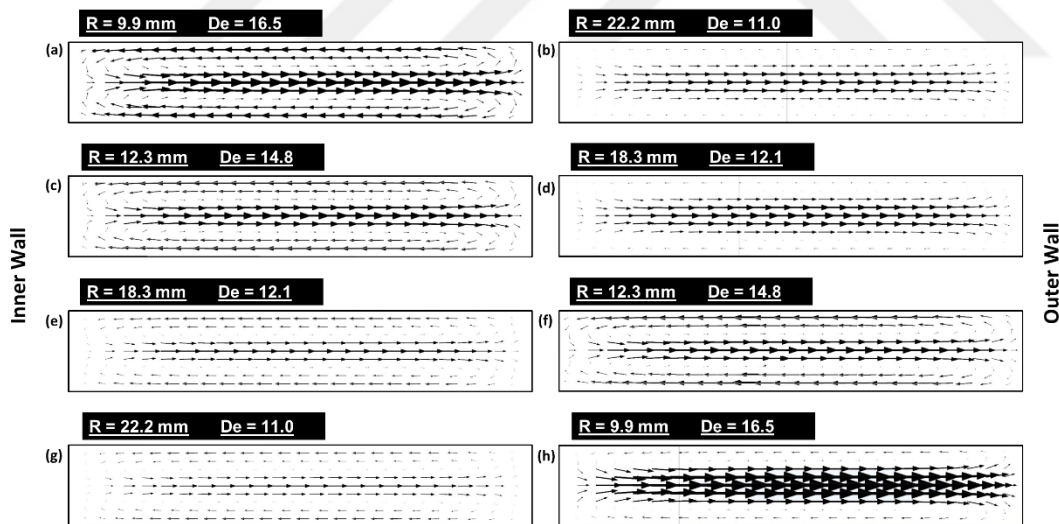


**Figure 4.2:** The variations of Dean velocity distribution at the beginning and at end of the last quarter loop of the channel for a and b) Case 1 (IAR=3:2), c and d) Case 2 (IAR=11:9), e and f) Case 3 (IAR=9:11), and g and h) Case 4 (IAR=2:3), respectively. The arrow lengths are proportional to the lateral velocity. The flow rate is 3mL/min.

As Case 1 and Case 4 have similar configurations, the arrow sizes representing the lateral velocity are similar as expected. The variation of curvature radius is greater in Case 1 and Case 4. Figure 4.2(a) and (h) (where the minimum radius, 9.9 mm, is

located) illustrates more intense arrows in the middle due to the increased centrifugal effects. Bold arrows show the enhancement of lateral migration, which makes the particles equilibrate faster. Figure 4.2 also reveals that the intensity of the arrows is less in Case 2 and Case 3 since the change of curvature radius is within a narrower range compared to Case 1 and Case 4. For example, Figure 4.2(a) (Case 1) and Figure 4.2(h) (Case 4) are expected to exhibit similar velocity distributions regarding the geometric similarity and the same Dean number. Since the plane of Figure 4.2(h) is located at the end of the curved section of the microchannel, the arrow intensities above and below the zero Dean velocity lines, which are defined in Figure 2.6(b)), start to reduce. This is due to the loss of Dean drag effect as the flow enters the straight section of the microchannel. Other cause for this kind of behavior is that the length of a quarter loop may not be long enough for the secondary flow to be fully developed. The same explanations apply to the rest as well.

Moreover, the arrows are generally less visible in Figure 4.2(b), (d), (e) and (g) compared to their components in the same row. The common feature of these subfigures is that they represent the cross-sections, which are located at the end of the quarter loop, where the curvature radius is increasing. The scale of the arrows is smaller at the top and bottom parts of the microchannels due to the fact that the tangential velocities decrease as a result of the increased radius of curvature. These findings lead to less effective migration in the transverse plane.

## **4.2 Lateral Positioning of Particle Streams**

### **4.2.1 Determination of optimum flow rates**

In this study, the elliptic spiral microchannels were employed with the use of 10  $\mu\text{m}$  and 20  $\mu\text{m}$  diameter particles. The particles were tested individually in each channel for several Reynolds numbers. At flow rates within the range of 0.5 mL/min-3.5 mL/min, fluorescent polystyrene particles diluted in deionized water were introduced into the microchannel through the inlet. For each case, channel Reynolds number,  $Re_C$ , was altered by increasing the flow rate, and the focusing positions of the particle streams in the diverged section prior to the 8-outlet-segment were recorded with respect to  $Re_C$ .

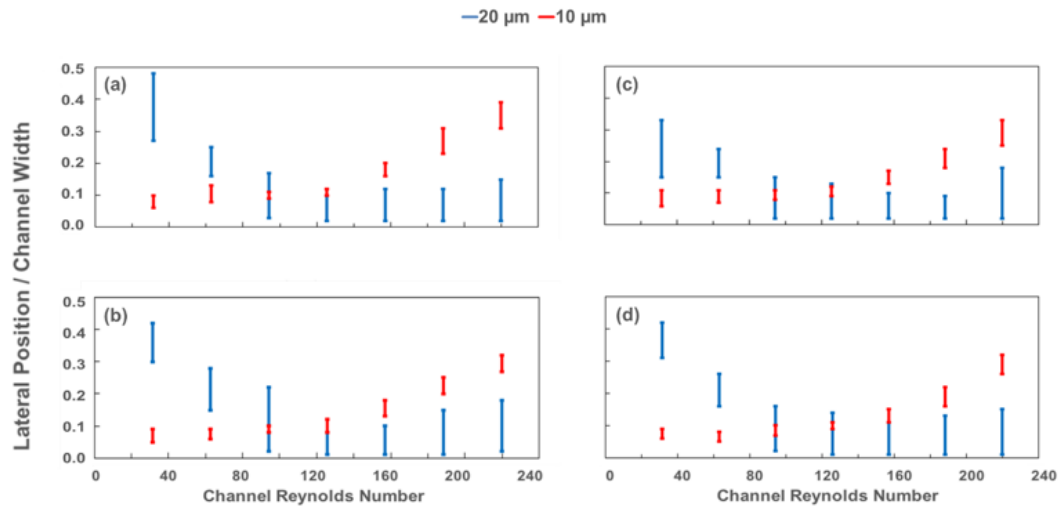


**Figure 4.3:** Lateral focusing position from the inside wall normalized by the channel exit width of 1mm for a) Case 1 (IAR=3:2), b) Case 2 (IAR=11:9), c) Case 3 (IAR=9:11) and d) Case 4 (IAR=2:3) at the outlet.

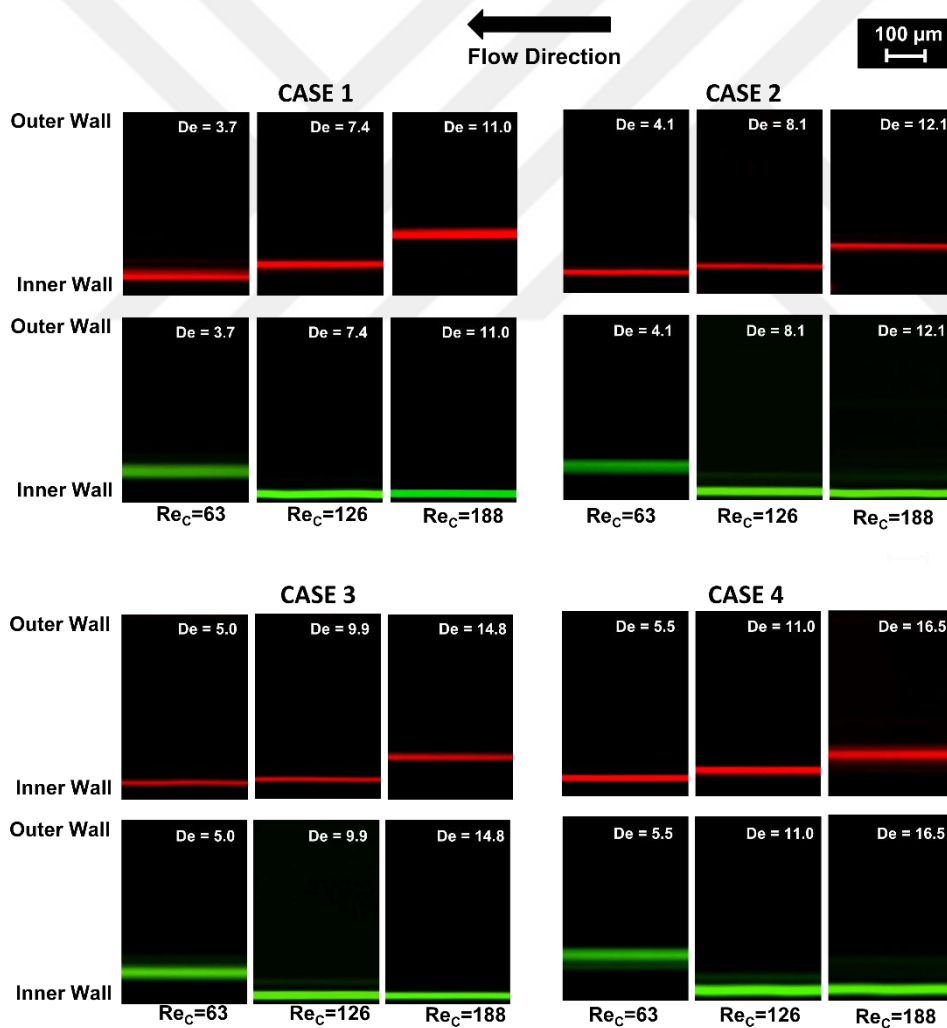


**Figure 4.4:** The trajectories of the particle streamlines at the end of the last spiral loop, where the channel width is 500 μm for 10 μm (red lines) and 20 μm (green lines) at  $Re_c$  of 63, 126 and 188 for a) Case 1 (IAR=3:2), b) Case 2 (IAR=11:9), c) Case 3 (IAR=9:11) and d) Case 4 (IAR=2:3).

By utilizing the recorded data of both 10- $\mu\text{m}$  and 20- $\mu\text{m}$  fluorescent particle streams at various flow rates, the ratio of lateral focusing positions to channel width at the exit is displayed as a function of the channel Reynolds number in Figure 4.3. In addition, the trajectories of the particle streams at the end of the last spiral loop before entering the outlet channel (for each particle size at  $Re_C$  of 63, 126 and 188) are demonstrated in Figure 4.4. After analyzing these results, the optimum flow rate required to achieve multi-particle separation was determined to investigate the sorting capability for later experiments. The optimum flow conditions assigned for each channel correspond to  $Re_C$  higher than 180 for all the cases.

## **4.2.2 Lateral focusing behavior of 10- $\mu\text{m}$ and 20- $\mu\text{m}$ particles**

### **4.2.2.1 Low range of flow rates ( $Re_C < 70$ )**

At lower  $Re_C$ , the larger particles are not precisely focused, while smaller particles are located closer to the inner wall. Due to the changing radius in the fabricated elliptic devices, the alternation of the curvature might complicate the flow pattern and disturbs the equilibrium of larger particles. Even though the lift force is supposed to be more dominant for larger particles, there may not be enough distance in the channel cross-section for 20- $\mu\text{m}$  particles to reach equilibrium positions unlike 10- $\mu\text{m}$  particles. Moreover, the lift coefficient for larger particles might be lower at lower volumetric flow rates. Thus, the secondary flow in the radial plane entrains the larger particles and generates distributed streams in the vicinity of the channel center when  $Re_C$  is smaller than 70. On the other hand, the mixing effects of the Dean drag are apparently surpassed by the lift forces for smaller particles at the lower flow rates. Therefore, the small particles migrates near the inner wall.

The results emphasize on the possibility of separation at lower  $Re_C$  due to non-overlapping focusing gaps, where the channel Reynolds number is less than 70. The focusing band is yet larger for 20  $\mu\text{m}$  particles, which makes it difficult to collect samples at a single outlet with the current configuration of the channel outlets. Besides, the mixing effects of the Dean drag is more dominant over the focusing behavior of the large particles, and the streamlines are more dispersed rather than focused. Hence, this might cause the particle-particle interaction and it is preferable to test the devices at higher flow rate.

#### 4.2.2.2 Mid-range of flow rates ( $70 < Re_C < 160$ )

As 20  $\mu\text{m}$  diameter particles yield higher  $a_p/D_h$  ratio, the net lift force acting on the particles causes constant stream positions so that the particles focus within a narrow band of streamlines near the inside wall for Reynolds numbers above 70. Meanwhile, the small particles move from the inner wall to the channel centerline, while large particles migrate contrarily towards the center of curvature with increasing  $Re_C$  (Figure 4.3 and Figure 4.4). As the channel velocity increases, the equilibrium positions of 20- $\mu\text{m}$  diameter particles begin to appear close to the innermost channel wall as a result of the superposition of inertial lift and Dean drag forces. 10  $\mu\text{m}$  particles move towards the channel center with increasing drag force.

In fact, the magnitude of the drag force is expected to increase less than the lift force with increasing velocity according to Eq. 2.1 and Eq. 2.2 ( $F_L \propto U^2$  and  $F_D \propto U^{1.63}$ ). Drag effects gaining dominance on the smaller particles with increasing flow rate might be explained by the reduction of the lift coefficient for the small particles under the given flow conditions.

Furthermore, the smaller particles align in considerably narrower streams for each case (Figure 4.3 and 4.4). In addition to the intrinsic size difference and non-normalized focus ranges with respect to particle dimension, this finding implies that the smaller particles are easier to be manipulated with the current channel height (aspect ratio). Figure 4.3 also reveals that both particles display overlapping streams in the middle  $Re_C$  range (from  $\sim 70$  to 160), which is not suitable for separation of particles with different sizes.

#### 4.2.2.3 High range of flow rates ( $160 < Re_C$ )

From Figure 4.3, it is apparent that the proposed elliptic channels offer separation capability at higher flow rates considering the narrow focus bands and the spacing between the streamlines of both particles. Accordingly, the optimal flow conditions are determined for each channel configuration to achieve the best particle separation. These conditions are  $Re_C=188$  (3.0mL/min) for Cases 1 and 2 and  $Re_C=195$  (3.1 mL/min) for Cases 3 and 4. The corresponding Dean numbers for the optimal operating conditions are 11, 12.2, 15.4 and 17, respectively, which all meet the criterion of  $De < 20$  for focusing [54, 79] and allow successful sorting of particles with sizes of 10 and 20  $\mu\text{m}$ . The optimum flow rates for separation of 10  $\mu\text{m}$  and 20  $\mu\text{m}$  particles

slightly increase for Case 3 and Case 4 compared to Case 1 and Case 2. Because, the proper gap between the focusing bands of the 10  $\mu\text{m}$  and 20  $\mu\text{m}$  particles forms at relatively greater  $Re_C$ .

20  $\mu\text{m}$  particles align near the inner wall and are collected by the first outlet tubing, while 10  $\mu\text{m}$  particles focus further from the inner wall and are recovered through the second outlet tubing. Apparently, the particles can be separated into parallel streamlines. Fluorescent images of each particle stream at optimum  $Re_C$  were captured at the channel outlet by utilizing the corresponding filters. The recorded images were superimposed in order to build a composite image showing the two particle streams simultaneously. As a result, Figure 4.5 was constructed to demonstrate a sample of the separation capability from Case 4 at  $Re_C=195$  (3.1 mL/min). The positions of focusing streamlines of both 10 $\mu\text{m}$  (red) and 20 $\mu\text{m}$  (green) particles are shown within the channel geometry (Figure 4.5).

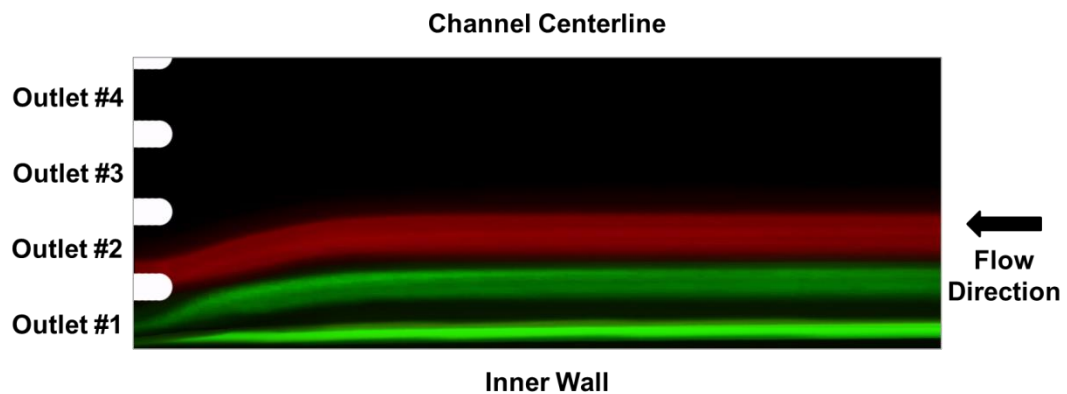


**Figure 4.5:** The superimposed fluorescent image of the focused streamlines: red (10 $\mu\text{m}$ ) and green (20 $\mu\text{m}$ ) illustrating particle migration for Case 4 (IAR=2:3) at the optimum flow conditions ( $Re_C=195$ ).

#### 4.2.3 Comparison of the focusing behavior of elliptic microchannels

Figure 4.4 reveals that the focused streamlines of 10  $\mu\text{m}$  and 20  $\mu\text{m}$  particles are relatively wider for Case 1 and Case 4 (Figure 4.4(a) and (d)), which have similar configurations. The radius of curvature changes in a more intense trend for these cases. This intense variation of curvature radius results in slightly spread streamlines compared to Case 2 and Case 3. On the other hand, thinner streamlines of the focused particles occur in Case 2 and Case 3 (Figure 4.4(b) and (c)), due to the fact that the curvature radius changes within a relatively narrow range. In addition, 10  $\mu\text{m}$  particles are aligned at locations closer to the channel centerline at  $Re_C= 188$  for Case 1 and

Case 4, where the variation of Dean drag force is larger compared to Case 2 and Case 3. This also emphasizes that the Dean drag forces are more effective in focusing behavior of 10  $\mu\text{m}$  particles at higher flow rates.

#### **4.2.4 The change of focusing behavior at the exit of straight outlet**

The streamlines of both particles are widened compared to Figure 4.4. Although, there is only one focused streamline for 20  $\mu\text{m}$  particles at the end of the last elliptic spiral loop as seen in Figure 4.4, two focused green streamlines are formed before the 8-branch outlet in Figure 4.5. The division of the focused green line and the widening of both red and green streamlines are triggered by the expanded outlet channel and the consequent drop of the aspect ratio and the downstream velocity. With the reducing velocity, the equilibrium of the large particles is starting to segregate according to the focusing behavior for the large particles at lower flow rates in Figure 4.3. Since the curvature end in the straight section of the microchannel, the Dean drag effects in the straight section also disappear and lead to the division of the green streamline. The green streamline adjacent to the inner wall is formed by the fraction of 20  $\mu\text{m}$  particles, which preserves the balance of  $F_D$  and  $F_L$  throughout the exit. On the other hand, the other pseudo-focused green line consists of the rest of the 20- $\mu\text{m}$  particles. Yet, both green streamlines are recovered from the outlet #1 as aimed.

### **4.3 Particle Separation Capability**

Under optimal conditions, the proposed microfluidic devices were tested until the focused particle streams form. Then, fractions of the streams were collected at all of the eight channel outlets, which were labeled starting from the inner wall. Following that, a particle counting procedure was conducted for every branch of the outlet. The composite image sections of the collected particle distributions at outlet #1 and outlet #2, used in particle counting, can be seen in Figure 4.6(a). Smaller specimens (as shown in Figure 4.6(a)) from each of the collected samples were examined by counting the particles manually with the utilization of the microscope software and ImageJ software tools. This process was repeated for several times for the sake of increasing the repeatability of the data.

After the amount of particles for each size was counted, the particle collection purities were obtained. There are particles detected in every output fraction. However, the total

amount of particles filtered at the outlets #1 and #2 covers a significant majority in each case. Therefore, a chart (Figure 4.7) could be generated only for the first and second outlets. The collected particles from each of the outlets were analyzed to quantify the particle collection purity, which is defined as the ratio of collected particles at particular outlets to the total collected particles. Approximately 0.01 v/v % volume fraction of particles was considered in the experiments. In addition, the ratio of the amount of the employed particles was 1:1.

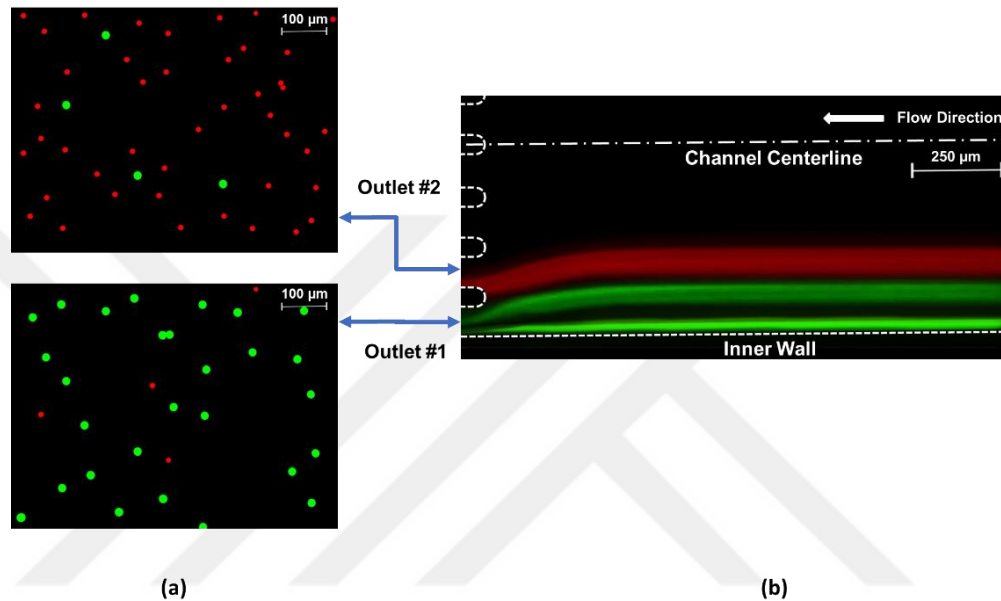


**Figure 4.6:** (a) The fluorescent microscopic views of samples utilized for particle counting and (b) the superimposed fluorescent image of two focused streamlines: red (10µm) and green (20µm) illustrating particle migration for Case 4 (IAR=2:3) at the optimum flow conditions ( $Re_C=195$ ).

Figure 4.7 demonstrates that the particle collection purity of larger particles is within the range of 90-95%, while smaller particles are collected with ~5% less purity. In addition, the particles filtered out at the outlet #1 and #2 cover 88-98% of the total purity. The maximum collection purities of 95.3% (Case 3) and 90.0% (Case 1) are achieved for 20- and 10-µm particles, respectively.

20-µm particles have a greater purity than 10-µm particles, which can be explained by the more dominant lift force acting on the larger particles at the specified flow rate. Additionally, the Dean drag force is more effective in the focusing regime of the smaller particles under the optimum flow conditions. The mixing effects of Dean flow induce relatively more dispersed migration of the smaller particles, which results in less purity.

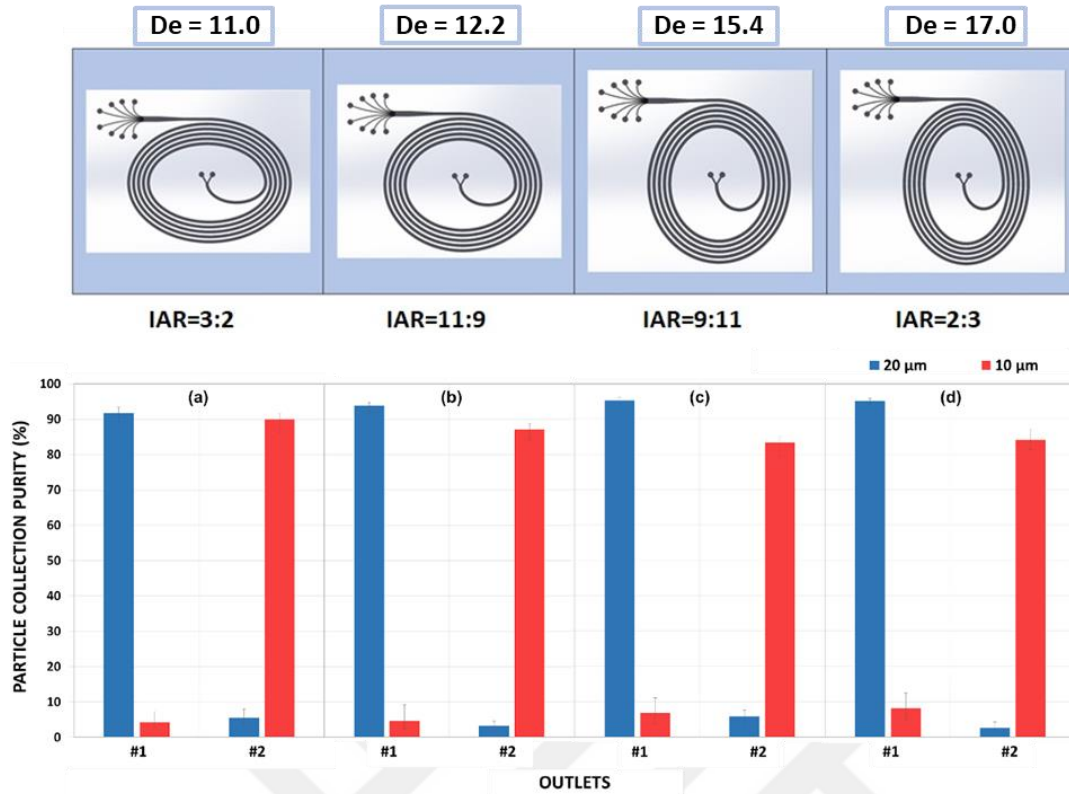


**Figure 4.7:** The particle separation purities obtained from the ratio of collected particles at particular outlets to the total collected particles for outlet #1 and #2 in a) Case 1 (IAR=3:2), b) Case 2 (IAR=11:9), c) Case 3 (IAR=9:11) and d) Case 4 (IAR=2:3).

Overall, all four cases yield a high particle collection purity for large 20- $\mu\text{m}$  particles: 91.9% (Case 1), 93.8% (Case 2), 95.3% (Case 3) and 94.9% (Case 4), with the assistance of successful focusing of small 10- $\mu\text{m}$  particles further from the inside wall. However, the purity of small 10- $\mu\text{m}$  particles is slightly less than larger particles: 90.0% (Case 1), 87.1% (Case 2), 83.4% (Case 3) and 84.0% (Case 4). The maximum purity is 90.0% for Case 1, while the minimum purity obtained in Case 3 is 83.4%. As  $F_D$  increases to the same order of magnitude as  $F_L$  for small particles, they are strongly influenced by the Dean drag force in the migration process. Due to the uneven flow distribution at the outlet openings, a considerably wider fraction of the flow channels into the outlet #1 compared to the second one as seen in Figure 4.6(b). This behavior also deteriorates the purity of the collected 10- $\mu\text{m}$  particles by raising the possibility of small particles to enter the first outlet.

At the optimum flow rates for all cases, the purity of 20- $\mu\text{m}$  particles collected at the first outlet is larger. On the other hand, 10- $\mu\text{m}$  particles can be well collected at outlet #2, yet relatively with less purity, which suggests that the Dean drag forces acting on

10  $\mu\text{m}$  particles are dominant. Thus, small particles are more defocused compared to larger ones. Additionally, the behavior of 20  $\mu\text{m}$  particles is dominated by the lift forces as the Dean velocities are significantly smaller in the proximity of the equilibrium positions/near the sidewalls. Thus, the focused large particles preserve their position.

Due to the alternating curvature along the last quarter loop of the microchannels, the ratio of  $F_D$  at the exit and at the beginning of the last quadrant loop varies for each channel.  $F_D$  decreases by nearly half in Case 1, where the exit is closer to the straight form and  $De = 11.0$ . This ratio almost doubles in Case 4, where the curvature radius is the smallest among all the cases and  $De = 17.0$  at the exit. In the light of this, a decrease in the purity of 10  $\mu\text{m}$  particles occurs with the increasing Dean number (Figure 4.7). Because some of the particles exhibit defocusing behavior and migrate to the undesired outlet openings. As the microchannel in Case 1 ( $De = 11.0$ ) is less affected by the varying Dean drag force, it yields the highest purity for 10  $\mu\text{m}$  particles. The lift forces dominate in inertial focusing of 20  $\mu\text{m}$  particles, and the gradual change in Dean flow is thus ineffective in terms of defocusing. Yet, the varying drag force stimulates the non-focusing large particles to shift toward the outlet #1, which enhances the purity of large particles with increasing  $De$  from Case 1 to Case 4.

#### 4.4 Discussion of the Experimental Results Regarding the Numerical Study

The lateral focusing positions as a function of channel Reynolds number in each channel are displayed in Figure 4.3 and 4.4. As explained earlier, the optimum flow rates enabling the separation of the employed particles slightly increase for Case 3 and Case 4 ( $Re_C = 195$ ) compared to Case 1 and Case 2 ( $Re_C = 188$ ). According to the distance size between the focused streamlines of the 10  $\mu\text{m}$  and 20  $\mu\text{m}$  particles, greater  $Re_C$  requires for Case 3 and Case 4.

In Cases 1 and 2, where  $IAR$  (Initial Aspect Ratio)  $> 1$ , particles with 10 $\mu\text{m}$  diameter remain near the inner wall up to Reynolds number of approximately 125. Beyond this critical  $Re_C$ , the Dean drag force becomes more dominant. Hence, the focusing band of the smaller particles shifts away from the inner wall. For Cases 3 and 4, where  $IAR < 1$ , the critical Reynolds number is slightly higher, above 150. This behavior is unexpected since the curvature radius of the last loop is larger and therefore Dean number is lower for Case 1 ( $De = 11.0$ ), and 2 ( $De = 12.2$ ), which are more prone to the

straight geometry than Cases 3 and 4. Consequently, Dean number is relatively smaller (Figures 2.8 and Figure 4.4), and Dean drag forces are expected to be less effective at the same  $Re_c$  for Cases 1 and 2. This finding can be explained by the curvature radius change through the last quarter loop. Even though the radius is smaller at the exit and Dean number is higher for Case 3 ( $De=15.4$ ), and Case 4 ( $De=17.0$ ), it decreases significantly along the last  $\frac{1}{4}$  turn. Therefore, the particles leave the last loop before the hydrodynamic forces are fully developed. This behavior was also observed in the numerical study. Based on Figure 4.2, it was interpreted that the length of a quarter loop might not be long enough for the secondary flow to be fully developed, and therefore for particles to entrain to their equilibrium positions before entering the straight section where the drag effects disappear. Additionally, the size of the radius grows to its maximum value in a rapid manner and consequently Dean number drops before the entrance of the straight exit channel in Cases 1 and 2. Similarly, the undeveloped forces lead the critical Reynolds number to differ for the elliptic channels with  $IAR > 1$  (Case 1 and 2) and  $IAR < 1$  (Case 3 and 4).

As presented in Figure 4.7, 20- $\mu\text{m}$  particles demonstrate better purity than 10- $\mu\text{m}$  particles, which suggests the dominance of the lift force acting on the larger particles at the specified flow rate. On the other hand, the focusing regime of the smaller particles are strongly influenced by the drag force under the optimum flow conditions. The mixing effects of Dean flow induce relatively more dispersed migration of the smaller particles that causes a reduction in purity. The difference between the particle collection purities of both particle sizes was larger (more than 10%) for Cases 3 and 4. The common feature these channels share is that the Dean number increases through the last quarter loop as  $IAR < 1$ . As explained earlier, the length of  $\frac{1}{4}$  loop fell short for the secondary flow to reach its steady state. This was observed in the numerical results as well in Figure 4.2 where the arrow intensities near the top and bottom walls indicate that the lateral rotation induced by the secondary flow is still processing to get to the fully developed regime. Due to the abovementioned reasons, a fraction of the small particles lose focusing and migrate to the undesired positions. Therefore, the defocused particles are collected by the designated outlets less efficiently. However, the same flow conditions might be beneficial for the collection purity of the large particles considering the highest purities are managed in Cases 3 and 4. As the lift force dominates the focusing of 20  $\mu\text{m}$  particles, the increasing Dean number is

ineffective in terms of defocusing. Yet, it might stimulate the unfocused fraction of the large particles to move toward the outlet #1 and enhance the separation yield of 20  $\mu\text{m}$  particles.





## 5. CONCLUSIONS

Different microfluidic devices with elliptic configurations were tested in this study to determine the optimum flow rates to accomplish particle focusing with high purity. These devices can separate suspending particles effectively due to the integration of elliptic geometry into their design, which enhances the rate of lateral particle migration to equilibrium positions and is also proven by large purity values. The results indicate that an inertial sorting of employed microparticles can be succeeded in the proposed microchannel configurations using passive separation methods without requiring any external force. Purity values are more than 90% for 20- $\mu\text{m}$  particles and 85% for 10- $\mu\text{m}$  particles, which implies that the particles can be effectively recovered at the corresponding outlets. In future, these devices could be suitable for live cell sorting applications as well.

Overall, the proposed devices demonstrate good separation performances for 10  $\mu\text{m}$  and 20  $\mu\text{m}$  particles. The capabilities of elliptic configurations are higher than the reported separation yields for particles with same sizes. 10  $\mu\text{m}$  and 20  $\mu\text{m}$  particles were collected at the designated outlets in a spiral device with purities less than 80% and 90% respectively [10]. Hence, the collection purities were improved with the elliptic devices for both particle sizes.

The elliptic spiral devices also have relatively smaller footprint areas compared to the spiral ones used in similar separation applications. These spiral separator devices utilizing particles with same or closer diameters have similar channel dimensions. Thus, the proposed elliptic microchannels occupy less projectional area due to either fewer number of loops [57, 67] or the pinched shape compared to the spiral counterparts [10]. In addition, the optimum flow rates achieved in this study are rather high, and thus shorter lengths would be enough for successful separation and be beneficial in terms of reducing the footprint of the devices even more by decreasing the number of spiral loops for this specific sorting application. In terms of working flow rates, the proposed configurations enable shorter process time as well. The determined flow rates for elliptic microchannels were 3.0 mL/min for Case 1 & 2, and 3.1 mL/min for Case 3 & 4. On the other hand, the devices reported for similar

applications employed flow rates of  $\sim 3.0$  mL/min [10],  $\sim 2.5$  mL/min [57], and  $\sim 2.3$  mL/min [69]. Therefore, it would take less time for the elliptic microchannels to process same sample volumes.

The spacing between the focusing bands of 10- and 20- $\mu\text{m}$  diameter particles was considerably wide at the optimum flow rate (above  $Re_C=180$ ). Thus, the width of the microchannel might be contracted to reduce the footprint of the device. On the other hand, this modification causes a larger aspect ratio. Thus, Dean drag effects could become more dominant, which is not desired for separation. Nevertheless, the gap between large and small particles along the lateral direction could allow separation of particles with closer diameters in the future.

As the base fluid, deionized water, which is a Newtonian fluid, is used in the experiments. Recent studies showed a highly efficient separation by taking the advantage of elasto-inertial effects of non-Newtonian fluids [88]. In addition, other investigations confirmed the potential of elastic lift in non-Newtonian fluids for separating particles with a much smaller size [89, 90] along with a wider range of flow rates [91, 92]. Therefore, the use of viscoelastic fluids will be considered as a future research direction.

Even though Case 3 (IAR=9:11) offers the maximum efficiency (with 95.3%) for 20  $\mu\text{m}$ , among the four cases, Case 1 achieves a purity value above 90% for each particle size. Thus, it is more advantageous to employ the elliptic configuration with initial aspect ratio of 3:2, namely Case 1, for sorting applications. However, Case 3 is more efficient for applications where specifically larger particles are required to be isolated. Similarly, Case 1 provides better capability for isolating smaller particles. Yet all of these devices generally propose fast and cost-effective cell/particle separation alternatives.

Since high purity of particle collection is quantitatively obtained for a single process/passage, even higher purity values are possible for a cascade mode (multiple passages). While this study provides valuable insight into the focusing mechanisms and purity performance for cases of spiral microchannels with alternating curvature radius, the scope could be well extended by investigating a variety of particle sizes and further examining inertial focusing dynamics along the whole length of the

microchannels. Finally, integration of a self micropump into the system would enhance the portability of the microfluidic devices.

Moreover, the microfiltration design demonstrated impracticality at this stage. The idea could be investigated profoundly by adapting new fabrication methods, using printers with higher resolution to improve the photomask quality and revising the parameters of microposts.

Overall, these elliptic devices could be utilized in the high-purity separation of micro-size particles/cells such as CTCs, blood cells, bacteria, viruses, etc. and easily customized for numerous cell/particle-sorting applications in biotechnology.





## REFERENCES

- [1] **Fidler, I. J.** (2003). The pathogenesis of cancer metastasis: the 'seed and soil' hypothesis revisited. *Nature Reviews Cancer*, 3(6), 453–458.
- [2] **Ashworth, T. R.** (1869). A case of cancer in which cells similar to those in the tumours were seen in the blood after death. *Aust Med J.*, 14, 146.
- [3] **Chaffer, C. L., & Weinberg, R. A.** (2011). A perspective on cancer cell metastasis. *Science*, 331(6024), 1559–1564.
- [4] **Yilmaz, M., & Christofori, G.** (2010). Mechanisms of motility in metastasizing cells. *Molecular Cancer Research*, 8(5), 629–642.
- [5] **Chiu, T.-K., Lei, K.-F., Hsieh, C.-H., Hsiao, H.-B., Wang, H.-M., & Wu, M.-H.** (2015). Development of a microfluidic-based optical sensing device for label-free detection of circulating tumor cells (CTCs) through their lactic acid metabolism. *Sensors*, 15(3), 6789–6806.
- [6] **Tan, S. J., Yobas, L., Lee, G. Y. H., Ong, C. N., & Lim, C. T.** (2009). Microdevice for the isolation and enumeration of cancer cells from blood. *Biomedical Microdevices*, 11(4), 883–892.
- [7] **Augustsson, P., Magnusson, C., Nordin, M., Lilja, H., & Laurell, T.** (2012). Microfluidic, label-free enrichment of prostate cancer cells in blood based on acoustophoresis. *Analytical Chemistry*, 84(18), 7954–7962.
- [8] **Tan, S. J., Lakshmi, R. L., Chen, P., Lim, W.-T., Yobas, L., & Lim, C. T.** (2010). Versatile label free biochip for the detection of circulating tumor cells from peripheral blood in cancer patients. *Biosensors and Bioelectronics*, 26(4), 1701–1705.
- [9] **Özbey, A., Karimzadehkhoei, M., Kocaturk, N. M., Bilir, S. E., Kutlu, O., Gozuacik, D., & Kosar, A.** (2019). Inertial focusing of cancer cell lines in curvilinear microchannels. *Micro and Nano Engineering*, 2(November 2018), 53–63. <https://doi.org/10.1016/j.mne.2019.01.002>
- [10] **Bhagat, A. A. S., Kuntaegowdanahalli, S. S., & Papautsky, I.** (2009). Inertial microfluidics for continuous particle filtration and extraction. *Microfluidics and Nanofluidics*, 7(2), 217–226.
- [11] **Wolfrum, F., Vogel, I., Fändrich, F., & Kalthoff, H.** (2005). Detection and clinical implications of minimal residual disease in gastro-intestinal cancer. *Langenbeck's Archives of Surgery*, 390(5), 430–441.

- [12] Naoe, M., Ogawa, Y., Morita, J., Omori, K., Takeshita, K., Shichijyo, T., ... Iwamoto, S. (2007). Detection of circulating urothelial cancer cells in the blood using the CellSearch System. *Cancer: Interdisciplinary International Journal of the American Cancer Society*, 109(7), 1439–1445.
- [13] Bidard, F.-C., Mathiot, C., Delalogue, S., Brain, E., Giachetti, S., De Cremoux, P., ... Pierga, J.-Y. (2010). Single circulating tumor cell detection and overall survival in nonmetastatic breast cancer. *Annals of Oncology*, 21(4), 729–733.
- [14] Pierga, J.-Y., Bidard, F.-C., Mathiot, C., Brain, E., Delalogue, S., Giachetti, S., ... Marty, M. (2008). Circulating tumor cell detection predicts early metastatic relapse after neoadjuvant chemotherapy in large operable and locally advanced breast cancer in a phase II randomized trial. *Clinical Cancer Research*, 14(21), 7004–7010.
- [15] Cristofanilli, M., Budd, G. T., Ellis, M. J., Stopeck, A., Matera, J., Miller, M. C., ... Terstappen, L. W. M. M. (2004). Circulating tumor cells, disease progression, and survival in metastatic breast cancer. *New England Journal of Medicine*, 351(8), 781–791.
- [16] Cohen, S. J., Punt, C. J., Iannotti, N., Saidman, B. H., Sabbath, K. D., Gabrail, N. Y., ... Miller, M. C. (2008). Circulating tumor cells, progression-free survival, and overall survival in metastatic colorectal cancer: A subgroup analysis of a large multicenter study. *J Clin Oncol*, 26(19), 3213–3221.
- [17] Pantel, K., Brakenhoff, R. H., & Brandt, B. (2008). Detection, clinical relevance and specific biological properties of disseminating tumour cells. *Nature Reviews Cancer*, 8(5), 329–340.
- [18] Healthcare, G. E. (2007). Ficoll-Paque Plus intended use for in vitro isolation of lymphocytes. *GE Healthcare, Uppsala, Sweden*.
- [19] Allan, A. L., & Keeney, M. (2010). Circulating tumor cell analysis: technical and statistical considerations for application to the clinic. *Journal of Oncology*, 2010.
- [20] Autebert, J., Coudert, B., Bidard, F.-C., Pierga, J.-Y., Descroix, S., Malaquin, L., & Viovy, J.-L. (2012). Microfluidic: an innovative tool for efficient cell sorting. *Methods*, 57(3), 297–307.
- [21] Yu, M., Stott, S., Toner, M., Maheswaran, S., & Haber, D. A. (2011). Circulating tumor cells: approaches to isolation and characterization. *Journal of Cell Biology*, 192(3), 373–382.
- [22] Yusa, A., Toneri, M., Masuda, T., Ito, S., Yamamoto, S., Okochi, M., ... Ichinosawa, Y. (2014). Development of a new rapid isolation device for circulating tumor cells (CTCs) using 3D palladium filter and its application for genetic analysis. *PloS One*, 9(2).

- [23] **Huang, S.-B., Wu, M.-H., Lin, Y.-H., Hsieh, C.-H., Yang, C.-L., Lin, H.-C., ... Lee, G.-B.** (2013). High-purity and label-free isolation of circulating tumor cells (CTCs) in a microfluidic platform by using optically-induced-dielectrophoretic (ODEP) force. *Lab on a Chip*, 13(7), 1371–1383.
- [24] **Mohamed, H., Murray, M., Turner, J. N., & Caggana, M.** (2009). Isolation of tumor cells using size and deformation. *Journal of Chromatography A*, 1216(47), 8289–8295.
- [25] **Coumans, F. A. W., van Dalum, G., Beck, M., & Terstappen, L. W. M. M.** (2013). Filter characteristics influencing circulating tumor cell enrichment from whole blood. *PloS One*, 8(4).
- [26] **Alix-Panabières, C., & Pantel, K.** (2013). Circulating tumor cells: liquid biopsy of cancer. *Clinical Chemistry*, 59(1), 110–118.
- [27] **Crosland-Taylor, P. J.** (1953). A device for counting small particles suspended in a fluid through a tube. *Nature*, 171(4340), 37–38.
- [28] **Fulwyler, M. J.** (1965). Electronic separation of biological cells by volume. *Science*, 150(3698), 910–911.
- [29] **Wu, T.-H., Chen, Y., Park, S.-Y., Hong, J., Teslaa, T., Zhong, J. F., ... Chiou, P.-Y.** (2012). Pulsed laser triggered high speed microfluidic fluorescence activated cell sorter. *Lab on a Chip*, 12(7), 1378–1383.
- [30] **Esmailsabzali, H., Beischlag, T. V, Cox, M. E., Parameswaran, A. M., & Park, E. J.** (2013). Detection and isolation of circulating tumor cells: principles and methods. *Biotechnology Advances*, 31(7), 1063–1084.
- [31] **Deng, G., Herrler, M., Burgess, D., Manna, E., Krag, D., & Burke, J. F.** (2008). Enrichment with anti-cytokeratin alone or combined with anti-EpCAM antibodies significantly increases the sensitivity for circulating tumor cell detection in metastatic breast cancer patients. *Breast Cancer Research*, 10(4), R69.
- [32] **Talasaz, A. H., Powell, A. A., Huber, D. E., Berbee, J. G., Roh, K.-H., Yu, W., ... Mindrinos, M. N.** (2009). Isolating highly enriched populations of circulating epithelial cells and other rare cells from blood using a magnetic sweeper device. *Proceedings of the National Academy of Sciences*, 106(10), 3970–3975.
- [33] **Liu, Z., Fusi, A., Klopocki, E., Schmittel, A., Tinhofer, I., Nonnenmacher, A., & Keilholz, U.** (2011). Negative enrichment by immunomagnetic nanobeads for unbiased characterization of circulating tumor cells from peripheral blood of cancer patients. *Journal of Translational Medicine*, 9(1), 70.
- [34] **Zborowski, M., & Chalmers, J. J.** (2011). Rare cell separation and analysis by magnetic sorting. *ACS Publications*.

- [35] **Hughes, A. D., & King, M. R.** (2010). Use of naturally occurring halloysite nanotubes for enhanced capture of flowing cells. *Langmuir*, 26(14), 12155–12164.
- [36] **Nagrath, S., Sequist, L. V, Maheswaran, S., Bell, D. W., Irimia, D., Ulkus, L., ... Muzikansky, A.** (2007). Isolation of rare circulating tumour cells in cancer patients by microchip technology. *Nature*, 450(7173), 1235–1239.
- [37] **Wang, S., Wang, H., Jiao, J., Chen, K., Owens, G. E., Kamei, K., ... Wu, H.** (2009). Three-dimensional nanostructured substrates toward efficient capture of circulating tumor cells. *Angewandte Chemie International Edition*, 48(47), 8970–8973.
- [38] **Stroock, A. D., Dertinger, S. K. W., Ajdari, A., Mezić, I., Stone, H. A., & Whitesides, G. M.** (2002). Chaotic mixer for microchannels. *Science*, 295(5555), 647–651.
- [39] **Zhang, C., Khoshmanesh, K., Mitchell, A., & Kalantar-Zadeh, K.** (2010). Dielectrophoresis for manipulation of micro/nano particles in microfluidic systems. *Analytical and Bioanalytical Chemistry*, 396(1), 401–420.
- [40] **Li, Y., Dalton, C., Crabtree, H. J., Nilsson, G., & Kaler, K. V. I. S.** (2007). Continuous dielectrophoretic cell separation microfluidic device. *Lab on a Chip*, 7(2), 239–248.
- [41] **MacDonald, M. P., Spalding, G. C., & Dholakia, K.** (2003). Microfluidic sorting in an optical lattice. *Nature*, 426(6965), 421–424.
- [42] **Sajeesh, P., & Sen, A. K.** (2014). Particle separation and sorting in microfluidic devices: a review. *Microfluidics and Nanofluidics*, 17(1), 1–52.
- [43] **Bain, B. J.** (2004). *A beginner's guide to blood cells(2nd Ed)*. London, UK: Blackwell Publishing.
- [44] **Seifter, J., Sloane, D., & Ratner, A.** (2005). *Concepts in medical physiology*. Philadelphia, USA: Lippincott Williams & Wilkins.
- [45] **Eichelberger, L. E., Koch, M. O., Eble, J. N., Ulbright, T. M., Juliar, B. E., & Cheng, L.** (2005). Maximum tumor diameter is an independent predictor of prostate-specific antigen recurrence in prostate cancer. *Modern Pathology*, 18(7), 886–890.
- [46] **Hofman, V. J., Ilie, M. I., Bonnetaud, C., Selva, E., Long, E., Molina, T., ... Piaton, E.** (2011). Cytopathologic detection of circulating tumor cells using the isolation by size of epithelial tumor cell method: promises and pitfalls. *American Journal of Clinical Pathology*, 135(1), 146–156.

- [47] **Park, S., Ang, R. R., Duffy, S. P., Bazov, J., Chi, K. N., Black, P. C., & Ma, H.** (2014). Morphological differences between circulating tumor cells from prostate cancer patients and cultured prostate cancer cells. *PLoS One*, 9(1).
- [48] **Low, W. S., Abas, W., & Bakar, W. A.** (2015). Benchtop technologies for circulating tumor cells separation based on biophysical properties. *BioMed Research International*, 2015.
- [49] **Chen, Z., Zhang, S., Tang, Z., Xiao, P., Guo, X., & Lu, Z.** (2006). Pool–dam structure based microfluidic devices for filtering tumor cells from blood mixtures. *Surface and Interface Analysis: An International Journal Devoted to the Development and Application of Techniques for the Analysis of Surfaces, Interfaces and Thin Films*, 38(6), 996–1003.
- [50] **Bhagat, A. A. S., Hou, H. W., Li, L. D., Lim, C. T., & Han, J.** (2011). Pinched flow coupled shear-modulated inertial microfluidics for high-throughput rare blood cell separation. *Lab on a Chip*, 11(11), 1870–1878.
- [51] **Hyun, K.-A., Kwon, K., Han, H., Kim, S.-I., & Jung, H.-I.** (2013). Microfluidic flow fractionation device for label-free isolation of circulating tumor cells (CTCs) from breast cancer patients. *Biosensors and Bioelectronics*, 40(1), 206–212.
- [52] **Inglis, D. W., Davis, J. A., Austin, R. H., & Sturm, J. C.** (2006). Critical particle size for fractionation by deterministic lateral displacement. *Lab on a Chip*. <https://doi.org/10.1039/b515371a>
- [53] **Holm, S. H., Beech, J. P., Barrett, M. P., & Tegenfeldt, J. O.** (2011). Separation of parasites from human blood using deterministic lateral displacement. *Lab on a Chip*, 11(7), 1326–1332.
- [54] **Russom, A., Gupta, A. K., Nagrath, S., Di Carlo, D., Edd, J. F., & Toner, M.** (2009). Differential inertial focusing of particles in curved low-aspect-ratio microchannels. *New Journal of Physics*, 11(7), 75025.
- [55] **Nivedita, N., Ligrani, P., & Papautsky, I.** (2017). Dean Flow Dynamics in Low-Aspect Ratio Spiral Microchannels. *Scientific Reports*. <https://doi.org/10.1038/srep44072>
- [56] **Di Carlo, D., Edd, J. F., Irimia, D., Tompkins, R. G., & Toner, M.** (2008). Equilibrium separation and filtration of particles using differential inertial focusing. *Analytical Chemistry*. <https://doi.org/10.1021/ac702283m>
- [57] **Lee, W. C., Bhagat, A. A. S., Huang, S., Van Vliet, K. J., Han, J., & Lim, C. T.** (2011). High-throughput cell cycle synchronization using inertial forces in spiral microchannels. *Lab on a Chip*, 11(7), 1359. <https://doi.org/10.1039/c0lc00579g>

- [58] **Özbey, A., Karimzadehkhoei, M., Akgönül, S., Gozuacik, D., & Koşar, A.** (2016). Inertial Focusing of Microparticles in Curvilinear Microchannels. *Scientific Reports*. <https://doi.org/10.1038/srep38809>
- [59] **Martel, J. M., & Toner, M.** (2014). Inertial Focusing in Microfluidics. *Annual Review of Biomedical Engineering*. <https://doi.org/10.1146/annurev-bioeng-121813-120704>
- [60] **Di Carlo, D.** (2009). Inertial microfluidics. *Lab on a Chip*. <https://doi.org/10.1039/b912547g>
- [61] **Martel, J. M., & Toner, M.** (2012). Inertial focusing dynamics in spiral microchannels. *Physics of Fluids*, 24(3), 32001.
- [62] **Zhang, J., Li, W., Li, M., Alici, G., & Nguyen, N. T.** (2014). Particle inertial focusing and its mechanism in a serpentine microchannel. *Microfluidics and Nanofluidics*, 17(2), 305–316. <https://doi.org/10.1007/s10404-013-1306-6>
- [63] **Di Carlo, D., Irimia, D., Tompkins, R. G., & Toner, M.** (2007). Continuous inertial focusing, ordering, and separation of particles in microchannels. *Proceedings of the National Academy of Sciences*, 104(48), 18892–18897.
- [64] **Lee, M. G., Choi, S., & Park, J. K.** (2011). Inertial separation in a contraction-expansion array microchannel. *Journal of Chromatography A*, 1218(27), 4138–4143. <https://doi.org/10.1016/j.chroma.2010.11.081>
- [65] **Choi, Y.-S., Seo, K.-W., & Lee, S.-J.** (2011). Lateral and cross-lateral focusing of spherical particles in a square microchannel. *Lab on a Chip*, 11(3), 460–465.
- [66] **Mukherjee, P., Wang, X., Zhou, J., & Papautsky, I.** (2019). Single stream inertial focusing in low aspect-ratio triangular microchannels. *Lab on a Chip*, 19(1), 147–157. <https://doi.org/10.1039/c8lc00973b>
- [67] **Guan, G., Wu, L., Bhagat, A. A., Li, Z., Chen, P. C. Y., Chao, S., ... Han, J.** (2013). Spiral microchannel with rectangular and trapezoidal cross-sections for size based particle separation. *Scientific Reports*. <https://doi.org/10.1038/srep01475>
- [68] **Choi, J. S., Piao, Y., & Seo, T. S.** (2013). Fabrication of a circular PDMS microchannel for constructing a three-dimensional endothelial cell layer. *Bioprocess and Biosystems Engineering*, 36(12), 1871–1878.
- [69] **Ghadami, S., Kowsari-Esfahan, R., Saidi, M. S., & Firoozbakhsh, K.** (2017). Spiral microchannel with stair-like cross section for size-based particle separation. *Microfluidics and Nanofluidics*, 21(7), 1–10. <https://doi.org/10.1007/s10404-017-1950-3>

- [70] Sun, J., Li, M., Liu, C., Zhang, Y., Liu, D., Liu, W., ... Jiang, X. (2012). Double spiral microchannel for label-free tumor cell separation and enrichment. *Lab on a Chip*, 12(20), 3952. <https://doi.org/10.1039/c2lc40679a>
- [71] Warkiani, M. E., Khoo, B. L., Wu, L., Tay, A. K. P., Bhagat, A. A. S., Han, J., & Lim, C. T. (2016). Ultra-fast, label-free isolation of circulating tumor cells from blood using spiral microfluidics. *Nature Protocols*, 11(1), 134.
- [72] Kwon, T., Yao, R., Hamel, J. F. P., & Han, J. (2018). Continuous removal of small nonviable suspended mammalian cells and debris from bioreactors using inertial microfluidics. *Lab on a Chip*, 18(18), 2826–2837. <https://doi.org/10.1039/c8lc00250a>
- [73] Zhou, J., Giridhar, P. V., Kasper, S., & Papautsky, I. (2013). Modulation of aspect ratio for complete separation in an inertial microfluidic channel. *Lab on a Chip*, 13(10), 1919–1929.
- [74] Segre, G., & Silberberg, A. J. (1962). Behaviour of macroscopic rigid spheres in Poiseuille flow Part 1. Determination of local concentration by statistical analysis of particle passages through crossed light beams. *Journal of Fluid Mechanics*, 14(1), 115–135.
- [75] Zhang, J., Yan, S., Yuan, D., Alici, G., Nguyen, N.-T., Warkiani, M. E., & Li, W. (2016). Fundamentals and applications of inertial microfluidics: a review. *Lab on a Chip*, 16(1), 10–34.
- [76] Amini, H., Lee, W., & Di Carlo, D. (2014). Inertial microfluidic physics. *Lab on a Chip*, 14(15), 2739–2761.
- [77] Feng, J., Hu, H. H., & Joseph, D. D. (1994). Direct simulation of initial value problems for the motion of solid bodies in a Newtonian fluid. Part 2. Couette and Poiseuille flows. *Journal of Fluid Mechanics*, 277, 271–301.
- [78] Hur, S. C., Henderson-MacLennan, N. K., McCabe, E. R. B., & Di Carlo, D. (2011). Deformability-based cell classification and enrichment using inertial microfluidics. *Lab on a Chip*, 11(5), 912–920.
- [79] Di Carlo, D., Edd, J. F., Humphry, K. J., Stone, H. A., & Toner, M. (2009). Particle segregation and dynamics in confined flows. *Physical Review Letters*. <https://doi.org/10.1103/PhysRevLett.102.094503>
- [80] Bhagat, A. A. S., Kuntaegowdanahalli, S. S., & Papautsky, I. (2008). Continuous particle separation in spiral microchannels using dean flows and differential migration. *Lab on a Chip*. <https://doi.org/10.1039/b807107a>
- [81] Ookawara, S., Higashi, R., Street, D., & Ogawa, K. (2004). Feasibility study on concentration of slurry and classification of contained particles by microchannel. *Chemical Engineering Journal*, 101(1–3), 171–178.

- [82] **Dean, W. R.** (1928). Fluid motion in a curved channel. *Proceedings of the Royal Society of London. Series A, Containing Papers of a Mathematical and Physical Character*, 121(787), 402–420.
- [83] **Berger, S. A., Talbot, L., & Yao, L. S.** (1983). Flow in curved pipes. *Annual Review of Fluid Mechanics*, 15(1), 461–512.
- [84] **Norouzi, M., & Biglari, N.** (2013). An analytical solution for Dean flow in curved ducts with rectangular cross section. *Physics of Fluids*, 25(5), 53602.
- [85] **Gossett, D. R., & Carlo, D. Di.** (2009). Particle focusing mechanisms in curving confined flows. *Analytical Chemistry*, 81(20), 8459–8465.
- [86] **Loutherback, K., D’Silva, J., Liu, L., Wu, A., Austin, R. H., & Sturm, J. C.** (2012). Deterministic separation of cancer cells from blood at 10 mL/min. *AIP Advances*, 2(4), 42107.
- [87] **Asmolov, E. S.** (1999). The inertial lift on a spherical particle in a plane Poiseuille flow at large channel Reynolds number. *Journal of Fluid Mechanics*, 381, 63–87.
- [88] **Nam, J., Lim, H., Kim, D., Jung, H., & Shin, S.** (2012). Continuous separation of microparticles in a microfluidic channel via the elasto-inertial effect of non-Newtonian fluid. *Lab on a Chip*, 12(7), 1347–1354.
- [89] **Lee, D. J., Brenner, H., Youn, J. R., & Song, Y. S.** (2013). Multiplex particle focusing via hydrodynamic force in viscoelastic fluids. *Scientific Reports*, 3, 3258.
- [90] **Kim, J. Y., Ahn, S. W., Lee, S. S., & Kim, J. M.** (2012). Lateral migration and focusing of colloidal particles and DNA molecules under viscoelastic flow. *Lab on a Chip*, 12(16), 2807–2814.
- [91] **Xiang, N., Zhang, X., Dai, Q., Cheng, J., Chen, K., & Ni, Z.** (2016). Fundamentals of elasto-inertial particle focusing in curved microfluidic channels. *Lab on a Chip*, 16(14), 2626–2635.
- [92] **Lim, E. J., Ober, T. J., Edd, J. F., Desai, S. P., Neal, D., Bong, K. W., ... Toner, M.** (2014). Inertio-elastic focusing of bioparticles in microchannels at high throughput. *Nature Communications*, 5(1), 1–9.

## CURRICULUM VITAE



**Name Surname** : KAAAN ERDEM

**Place and Date of Birth** : BANDIRMA / 02.10.1988

**E-Mail** : erdemk@itu.edu.tr

### **EDUCATION** :

**B.Sc.**, 2010, ITU, Faculty of Mechanical Engineering, Mechanical Engineering Program

**M.Sc.**, 2012, ITU, Graduate School of Science Engineering and Technology, Mechanical Engineering Department, Heat-Fluid Graduate Program

### **PUBLICATIONS, PRESENTATIONS AND PATENTS ON THE THESIS:**

- **Erdem, K.**, Ahmadi, V. E., Kosar, A., & Kuddusi, L. (2020). Differential Sorting of Microparticles Using Spiral Microchannels with Elliptic Configurations. *Micromachines*, 11(4), 412.

### **OTHER PUBLICATIONS, PRESENTATIONS AND PATENTS:**

- Raheem, D. G., **Erdem, K.**, & Hasan, K. (2018). Techno-environmental studies on a reciprocating internal combustion engine fired with syngas produced by gasifying different types of Turkish lignites. *Int. J. Adv. Automot. Technol.*, 2(3), 137-142.

